Advanced Powder Technology 32 (2021) 3689–3705

Contents lists available at ScienceDirect

Advanced Powder Technology

journal homepage: www.elsevier.com/locate/apt

Original Research Paper

# Numerical simulation of a 3-D gas-solid fluidized bed: Comparison of TFM and CPFD numerical approaches and experimental validation

J.I. Córcoles [a,b], A. Acosta-Iborra [c], J.A. Almendros-Ibáñez [a,b,*], C. Sobrino [c]

[a] Universidad de Castilla-La Mancha, E.T.S. de Ingenieros Industriales, Dpto. de Mecánica Aplicada e Ingeniería de Proyectos, Campus universitario s/n, 02071 Albacete, Spain
[b] Universidad de Castilla-La Mancha, Renewable Energy Research Institute, Section of Solar and Energy Efficiency, C/ de la Investigación s/n, 02071 Albacete, Spain
[c] Universidad Carlos III de Madrid, ISE Research Group, Thermal and Fluids Engineering Department, Avda. de la Universidad 30, 28911 Leganés, Madrid, Spain

ARTICLE INFO

*Article history:*
Received 18 March 2021
Received in revised form 13 August 2021
Accepted 19 August 2021
Available online 4 September 2021

*Keywords:*
Fluidized bed
Numerical simulation
Computational particles fluid dynamic
Bubbles

ABSTRACT

This paper presents the results of a 3-D numerical simulation of a freely bubbling fluidized bed, based on the Eulerian–Lagrangian approach, using the software Barracuda (CPFD-Barracuda). The main results obtained were assessed in terms of frequency analysis, bubble pierced length, bubble size, bubble passage frequency and bubble velocity. The results obtained were also compared with experimental data obtained in a 3-D fluidized bed using pressure and optical probes, and with the numerical results using the more common Eulerian-Eulerian approach, implemented in the commercial software Fluent (TFM-Fluent).

The results show that CPFD-Barracuda satisfactorily predicts the global behaviour of bubbling beds with a low computational cost, although it computes smaller bubble sizes and lower bubble velocities than TFM-Fluent and experiments. Additionally, the spectra of pressure and particle volume fraction obtained with CPFD-Barracuda resemble those from the experiments and the TFM-Fluent simulations, but with a larger contribution of lower frequencies. The peaks of the pressure spectra from CPFD-Barracuda are close to those from the experiments and the TFM-Fluent simulations, whereas those in the solid volume spectra seem to be underestimated by CPFD-Barracuda. The results also indicate that the particle fraction threshold value chosen to distinguish bubbles contours notably influences the results of the bubble characteristics, especially for TFM-Fluent, whereas CPFD-Barracuda is less sensitive to this threshold value.



## 1. Introduction

Fluidized beds are one of the most widely used particle–fluid technologies in a multitude of applications in several industries. They have been used as combustors and gasifiers of coal and biomass [1–3] and many other industrial processes, such as in the pharmaceutical industry [4]. More recently, fluidized beds have also been proposed as a promising alternative to packed beds for solar thermal energy storage, especially for thermochemical and concentrated solar energy applications. The higher heat and mass transfer rates of fluidized beds over fixed beds makes them a more suitable technology [5]. In this context, there is great interest in the development of numerical models that permit bubbling fluidized beds to be simulated in large-scale industrial facilities with a reasonable computational cost.

Most computational fluid dynamics (CFD) models applied to multiphase flow find it difficult to properly describe the interactions between phases, which is a complex task when using two-phase flows [6]. Two different widely used approaches to model multiphase particle flows can be defined: two-fluid models (TFM), based on the Eulerian-Eulerian approach, and discrete particle model (DPM), based on the Eulerian–Lagrangian approach. TFM consider gas phase and particulate phase as two interpenetrating continua [7]. According to Grace and Taghipour [8], obtaining accurate solutions for multiphase flows is more challenging than for single-phase flows, because certain aspects should be taken into consideration to validate the numerical results, such as to consider particles as perfectly spherical, which might reduce the accuracy of interparticle and interphase stresses, or the influence of the mesh resolution on the accuracy of large gradients appearing at the bubble boundary. Several studies have reported

* Corresponding author at: Universidad de Castilla-La Mancha, E.T.S. de Ingenieros Industriales, Dpto. de Mecánica Aplicada e Ingeniería de Proyectos, Campus universitario s/n, 02071 Albacete, Spain.
*E-mail address:* jose.almendros@uclm.es (J.A. Almendros-Ibáñez).

https://doi.org/10.1016/j.apt.2021.08.029

that TFM overestimates the bed expansion in a bubbling bed of fluid catalytic cracking (FCC) particles [9,10], which might be improved including particle size distribution in the CFD models [11]. One of the most common simplifications assumed in TFM is that particles are considered to have the same diameter, density and coefficient of restitution, which might reduce the accuracy of the interparticle and interphase stresses [12]. Consideration of different particles in TFM would complicate the computational cost, because continuity and momentum equations should be solved for each size bin separately in the whole numerical domain. Another aspect to consider in TFM models is the accuracy of the results, which depends on the grid size, while the use of fine grids makes it difficult to solve 3-D computational domains with a reasonable computational cost. Recent studies indicate that the grid size to particle diameter ratio should be lower enough to properly reproduce the macrosocopic behaviour of the bed when particle clustering appears [13]. Some authors proposed values of this ratio lower than 10 [14]. Nikolopoulos et al. [13] indicate that particle aggregates may be relevant in either Geldart A or B particles. The reduction in the grid size increases the computational cost of TFM models.

An alternative to TFM are DPM, which can be classified in three different approaches: discrete element model (DEM), dense discrete phase model (DDPM) and multiphase particle in cell (MP-PIC). DEM track individual particles in time, and the particle phase is described as discrete and solved according to Newton's laws of motion to every particle. DEMs show a reliable description of the particle–particle collisions and are highly useful for the study of flow details in fluidized beds [15]. Therefore, DEMs require high computing power on tracking each particle trajectory and considering contact collisions of particles [16], and the number of computational particles used ($\approx 10^5$) is lower than the number of particles normally used in real industrial fluidized beds. Recent advances in this numerical approach rely on the use of the Energy Minimization Multi-Scale (EMMS) model for the drag coefficient, as it has been proved to better describe the operation of Circulating Fluidized Beds (CFB). The EMMS model improves the simulation when there are clusters of particles with dimensions smaller than the size of the computational cell, compared with conventional Gidaspow's drag model [17]. An approach to reduce the computational cost of DEM is DDPM, in which the particles are grouped in groups of particles (called parcels or clouds). In this approach, the particle–particle interactions are modeled with the Kinetic Theory of Granular Flow (KTGF). There are few studies in the literature [18,19] that studied the influence of different modeling parameters on the simulation of different fluidization regimes: bubbling, turbulent and circulating fluidized beds. Adnan et al. [19] concluded that EMMS/bubbling drag model predicts better the effects of dissipative structures than the conventional Gidaspow drag model.

Another alternative to DEMs is the multiphase particle in cell method, solving the momentum equation for computing particles, defined as a group of particles with the same properties i.e., parcels, rather than for individual particles as DEMs do, which allows the computational time to be notably reduced [20]. MP-PIC and DDPM conceptually are very similar, although there are some differences between them (apart from to simulate individual or grouped particles). MP-PIC usually uses simple relations for the solid stress, neglecting the shear stresses [21], which is usually included in DDPM; MP-PIC models the particle–particle interactions with the solid stress tensor equation, rather than with the KTGF, as DDPM does [19]; and there are also multiple differences in the numerical implementation [21]. Drawing on the MP-PIC method, a new Eulerian–Lagrangian CFD approach was created (computational particle fluid dynamics, CPFD) [22], which allows simulating large-scale industrial multiphase flow systems with a low computational cost, being able to reach real particle number of $10^{16}$ order of magnitude. MP-PIC is useful to compute particle stress gradient, which is difficult to solve for individual particles [23]. Another point to highlight is that it is enough to use coarse cartesian mesh, because there must be sufficient room in adjacent cells to accommodate any parcels that move into them in a subsequent time step [24].

Several studies have focused on the use of CPFD applied to industrial applications [25], such as down flow reactors [26], biomass combustion chambers [27], spouted beds [16], cold pilot calciners [28], and biomass gasification [29], among others. Other studies have applied CPFD to fluidized beds. Some researchers applied this method in 3-D models to study the effect of particle distribution in industrial circulating fluidized bed risers [30] and downers [31], and cylindrical beds [32]. Karimipour and Pugsley [6] analysed the capacity of the MP-PIC approach to model a 3-D bubbling fluidized bed of Geldart-A particles applied to FCC catalyst, analysing three different grid sizes and two drag models. They reported that the influence of the drag model is much lower than the effect of the grid size. Other studies applied CPFD to study the minimum fluidization velocity [33] in fluidized beds. Lim et al. [34] carried out a 2-D simulation to analyse the bed pressure drop and bubble flow behaviour of bubbling fluidized beds produced using a shroud nozzle distributor. Their findings were consistent with the observed experimental results when the most adequate collision model was selected. Yang et al. [35] simulated flow characteristics of Geldart A particles in bubbling fluidized bed with and without perforated plates implementing a 3-D model. They concluded that the results of predicting the gas–solid flow were not good enough compared with the experimental data and they proposed that the detailed structure of the fluid dynamics should be analysed carefully and not only solid volume fraction profiles.

Few studies have analysed a fluidized bed using a 3-D CPFD model and validated its results of hydrodynamics behaviour with experiments. In the aforementioned studies, some of them compared the numerical results with correlations for bubble properties, which might not be adequate for predicting the small bubbles that appear in Geldart A particles fluidization [6], or they compared the numerical results with experimental data of other studies, but only focused on solid fraction, bubble diameter and bubble velocity. Besides, there are works mainly focused on analysing solid volume fraction, axial particle velocity and particle residence time [30]. Alternatively, some studies have analysed a 2-D fluidized bed. In this regard, Liang et al. [23] carried out a critical validation study on the 2-D CPFD model in simulating gas–solid bubbling in fluidized bed. They compared their simulation results with the 2-D TFM model and experimental data of Hernández-Jiménez et al. [36], who used particle image velocimetry technique and digital image analysis in 2-D fluidized bed. In both studies, to analyse bubble and emulsion phases, the same arbitrary threshold particle volume fraction of 0.3 was considered. The authors concluded that the CPFD model predicted better profiles of solid velocity, but failed to properly simulate the bubble coalescence, suggesting that the parcel number utilized should be at least an order of magnitude lower than the real particle number. Shi et al. [37] studied the effect of model dimensionality (2D versus 3D) on the validation of fluidized bed models concluding that only the 3D simulations allow obtaining physically realistic results that are less sensitive to a choice of numerical parameters.

It is further required to carry out studies aimed at validating CPFD, to study its applicability to fluidized beds. With this aim, this paper presents the results of a numerical simulation for a freely bubbling fluidized bed, using the CPFD model. As a novelty, the CPFD model is applied to a 3-D domain and a broad analysis of

the fluidized bed hydrodynamics is performed. Moreover, results comprising frequency analysis, bubble pierced length, bubble size, bubble passage frequency and bubble velocity are compared with experimental data taken from a bed with the same geometry and operated under the same conditions [12]. These results are also compared with the numerical results of a 3-D model using the most common Two Fluid Model, implemented in the commercial software Fluent (TFM-Fluent) [38] for different values of the threshold value to detect bubbles contour. Hence, the numerical simulation was performed using a computational domain with geometry that can contribute to extrapolate the results in actual applications. Moreover, the influence of the temporal step, number of cells and threshold value on the results obtained with the Barracuda software (CPFD-Barracuda Virtual Reactor v. 17.3.1) is studied.

## 2. Experimental data

This section presents a brief description of the experiments carried out by Acosta-Iborra et al. [12]. In their study, a bubbling fluidized bed (inner diameter of 193 mm and height of 800 mm), filled with Geldart-B silica sand particles (with a mean particle size of $d_p = 540\,\mu$m), with an initial height ($H_{bed}$) of 0.22 m was studied. For the experiments, the superficial fluid velocity ($u_f$) in the bed was set to 0.57 m/s, which guaranteed fully bubbling conditions because the minimum fluidization velocity ($u_{mf}$) experimentally measured was 0.4 m/s. At the bottom inlet, air was distributed through a distributor plate, perforated with 90 holes of 2 mm diameter, to achieve homogeneous bubble generation. To detect the bubble passage along the height of the bed from the distributor and for different radial positions, several pressure and optical probes were installed at different locations inside the bed, yielding measurements of 10 min duration at a sampling frequency of 500 Hz.

## 3. Numerical model

### 3.1. Simulated bed with TFM-Fluent

In a previous study carried out by Acosta-Iborra et al. [12], a computational study on the bubble behaviour in a 3-D fluidized bed was performed, where the results obtained from experimental measurements were compared to the numerical results performed with the CFD software ANSYS Fluent 6.3 [39]. The 3-D computational domain was discretized with a structured grid (28,800 hexahedral cells). As boundary conditions, at the inlet, a uniform velocity was defined (0.57 m/s) for air at 25 °C, with a constant static pressure ($10^5$ Pa) at the outlet of the cylinder, because the top of the bed was open to the exterior air. At the lateral wall, a non-slip condition for the air was imposed. For the particles, a free-slip condition was defined at the wall because, in this kind of bed, particles are well fluidized and do not remain attached to the wall and, for simplicity, the drag of the wall on the particles can be neglected. In their study, an implicit finite volume technique (phase coupled SIMPLE) based on an iterative pressure correction was used to solve the governing equations, and using a second order discretization in space and time. The Gidaspow's drag model was used to take into account the momentum interchange between gas and particles. The main parameters defined for the numerical solution of Acosta-Iborra et al. [12] are shown in Table 1. More details of the equations and the numerical model are described by Acosta-Iborra et al. [12].

**Table 1**
Parameters of the TFM-Fluent simulation of Acosta-Iborra et al. [12].

| Parameter | Value |
|---|---|
| Time step (s) | $2.5\,10^{-4}$ |
| Iterations per time step | 40 |
| Maximum pack volume fraction (dimensionless) | 0.555 |
| Coefficient of restitution (dimensionless) | 0.9 |
| Angle of internal friction (degrees) | 30 |

### 3.2. Bed Simulated with CPFD-Barracuda

#### 3.2.1. Governing equations

The governing equations of the MP-PIC for the continuum phase (Eq. (1) and Eq. (2)) [40] and the particle phase (Eq. (3)) [20] are as follows:

Continuity equation:

$$\frac{\partial\left(\theta_f\,\rho_f\right)}{\partial t} + \nabla\cdot\left(\theta_f\,\rho_f\,\vec{u}_f\right) = 0 \tag{1}$$

Momentum equation:

$$\frac{\partial\left(\theta_f\,\rho_f\,\vec{u}_f\right)}{\partial t} + \nabla\cdot\left(\theta_f\,\rho_f\,\vec{u}_f\,\vec{u}_f\right) = -\nabla p - \vec{F} + \theta_f\,\rho_f\,\vec{g} + \nabla\cdot\left(\theta_f\,\tau_f\right) \tag{2}$$

$$\frac{d\vec{u}_p}{dt} = D_p\left(\vec{u}_f - \vec{u}_p\right) - \frac{1}{\rho_p}\nabla p - \frac{1}{\theta_p\,\rho_p}\nabla\cdot\tau_p + \vec{g} \tag{3}$$

where $\theta_f$ is the fluid volume fraction, $\rho_f$ is the fluid density, $u_f$ is the fluid velocity, p is the pressure, $F$ is the momentum exchange rate per volume between gas and particles, $g$ is the gravity acceleration, $\tau_f$ is the viscous stress term, $u_p$ is the particle velocity, $D_p$ is the drag function, $\rho_p$ is the particle density, $\theta_p$ is particle volume factor, and $\tau_p$ is the solid contact stress, which is computed as follows:

$$\tau_p = \frac{P_s\,\theta_p^{\beta}}{max\left[\left(\theta_{cp} - \theta_p\right), \varepsilon\left(1 - \theta_p\right)\right]} \tag{4}$$

where $P_s$ is the pressure constant, $\beta$ is a constant, $\theta_{cp}$ is particle volume fraction at close packing, and $\varepsilon$ is a constant. The default values used for the constants are $P_s = 1$ Pa, $\varepsilon = 10^{-8}$ and $\beta = 3$, which is recommended to be in the range of 2 to 5 [23,27].

The momentum exchange rate $\vec{F}$ in Eq. (2) is computed as follows:

$$\vec{F} = \iiint f\,V_p\,\rho_p\left[D_p\left(\vec{u}_f - \vec{u}_p\right) - \frac{1}{\rho_p}\nabla P\right] dV_p\,d\rho_p\,d\vec{u}_p \tag{5}$$

In the above equation, $V_p$ is the particle volume and $f$ represents the particle probability distribution function, which is computed using the Liouville equation for the particle position without a collision model:

$$\frac{\partial f}{\partial t} + \nabla\cdot\left(f\,\vec{u}_p\right) + \nabla_{\vec{u}_p}\cdot\left(f\,\frac{d\vec{u}_p}{dt}\right) = 0 \tag{6}$$

where $\nabla_{\vec{u}_p}$ is the divergence operator with respect to velocity. The flow is considered isothermal and the changes in the air density are computed with equation of state of the ideal gas:

$$P = \rho_f\,R_g\,T \tag{7}$$

where $R_g$ is the gas constant and $T$ the absolute temperature.

#### 3.2.2. Drag model

With regard to the drag model, the drag force exerted on the particle ($F_p$) depends on the fluid conditions, on the gas-particle

drag coefficient and on the Reynolds number and can be computed as follows:

$$F_p = m_p C_d |u_f - u_p| \tag{8}$$

where $m_p$ is the mass of the particle, and $C_d$ is the gas-particle drag coefficient

Several models are proposed to compute the drag force on solid particles. In the present study, the Wen-Yu model drag force [41] was used, which is expressed as follows:

$$D_p = 0.75 C_d \frac{\rho_f |u_f - u_p|}{\rho_p d_p} \tag{9}$$

and

$$C_d = \frac{24}{Re}\theta_f^{-2.65} \quad for \quad Re < 0.5 \tag{10}$$

$$C_d = \frac{24}{Re}(1 + 0.15 Re^{0.687})\theta_f^{-2.65} \quad for \quad 0.5 \leqslant Re \leqslant 1000 \tag{11}$$

$$C_d = 0.44\,\theta_f^{-2.65} \quad for \quad Re > 1000 \tag{12}$$

where $d_p$ is the particle diameter, and $Re$ is the Reynolds number.

To compute the particle drag, the Reynolds number is defined as:

$$Re = \frac{\rho_f |u_f - u_p| d_p}{\mu_f} \tag{13}$$

where $\mu_f$ is the dynamic viscosity of the fluid.

*3.2.3. Numerical setup*

The physical and geometrical parameters included in the CPFD Barracuda software were similar to those used in the study by Acosta-Iborra et al. [12]. Therefore, the computational domain studied using CPFD was a 3-D model, with an inner diameter and height of 193 mm and 800 mm, respectively (Fig. 1). Two grids were implemented to analyse the main results obtained, both of which were based on a uniform grid in directions x, y and z, resulting in a 45,980 cells (Coarser Grid) and 93,296 cells (Finer Grid). Fig. 2 shows a detail of the two grids. As can be observed, CPFD-Barracuda generates a general rectangular domain in the plane $x - y$ with uniform computational cell sizes in the three directions. In consequence, some cells are not in the domain. The number of real cells within the physical domain of the bed is indicated in Table 2.

For the bed, Geldart-B silica sand particles with an initial height of 0.22 m were used, with an initial particle volume fraction at close packing of $\theta_{cp} = 0.55$ and a real density of $2632.5\,kg/m^3$. The particles were of a uniform size ($540\,\mu m$ diameter) with a sphericity of $\Psi_p = 0.8$. Air enters the domain through the bottom inlet of the bed. The top outlet of the bed is connected to the exterior air at atmospheric conditions (25 °C). At the inlet, a constant superficial gas velocity of 0.57 m/s was defined with an isothermal flow temperature of 298.15 K.

With regard to the particle to wall interaction, default values for parameters such as normal-to-wall momentum retention (0.85), tangent to wall momentum retention (0.85) and diffuse bounce (5) were defined according to [42].

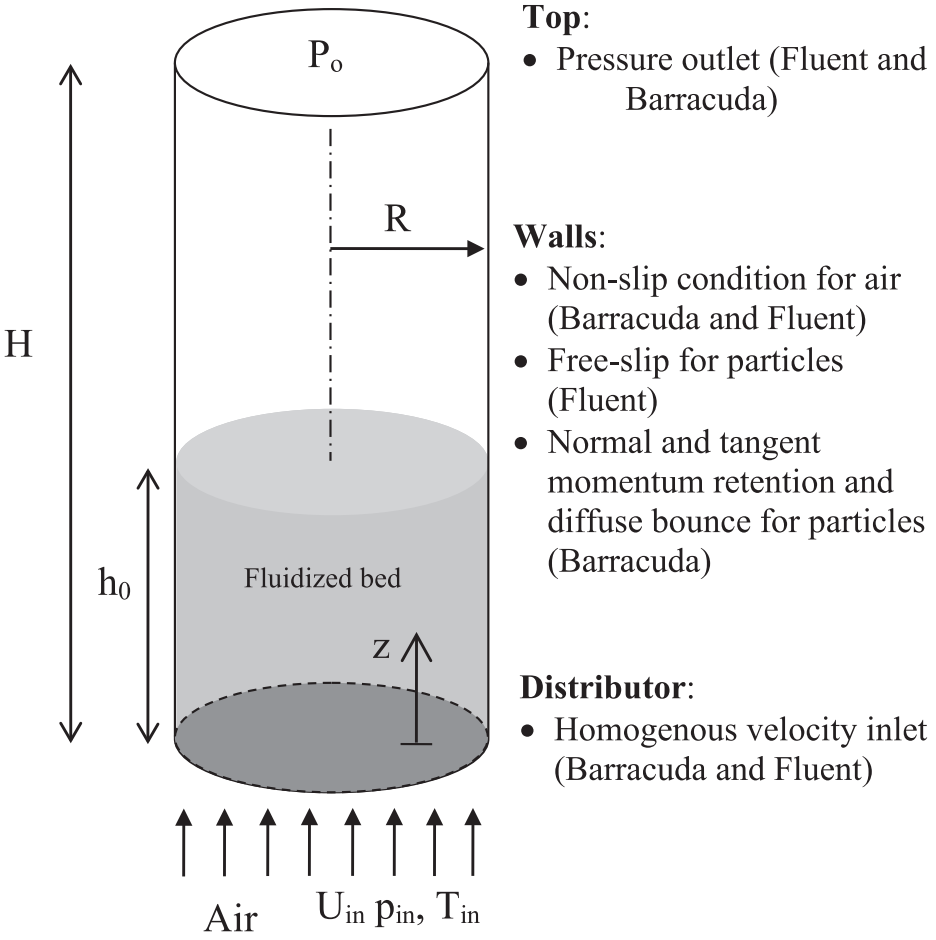


**Fig. 1.** CPFD model of the fluidized bed.

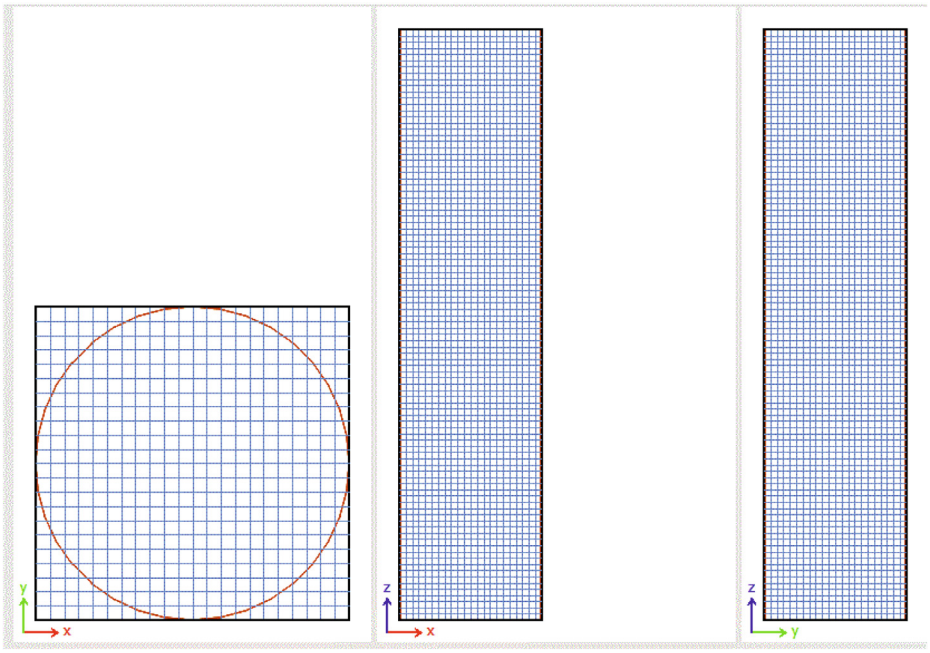

(a) Coarser grid of Cases 1 and 3

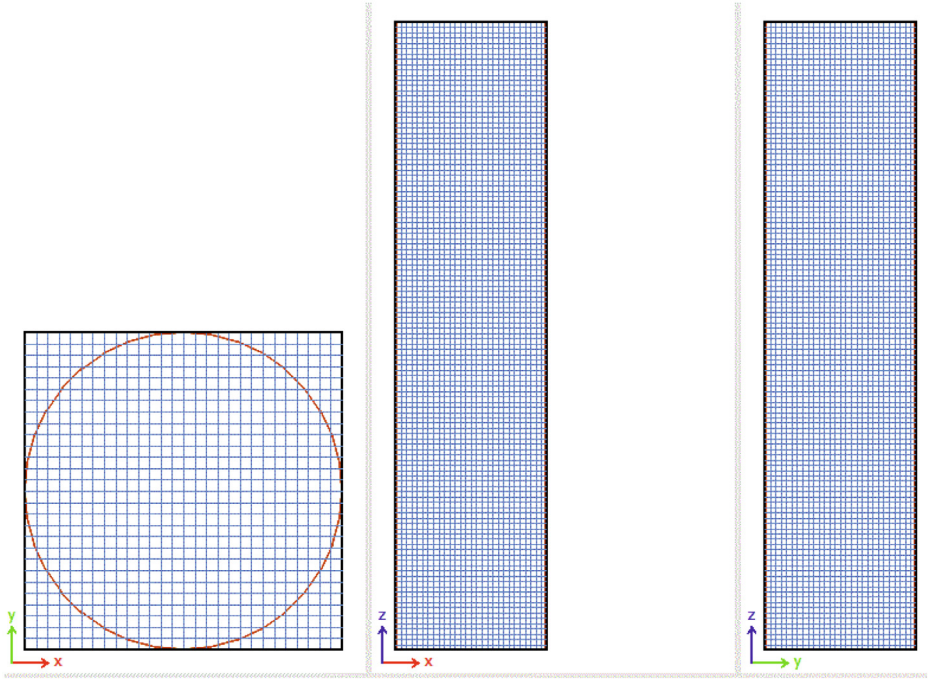

(b) Finer grid of Cases 2 and 4

**Fig. 2.** Detail of the two grids studied.

At each of the two proposed grids, two time steps were used, $10^{-3}$ s and $10^{-4}$ s, whereas the numerical simulations were performed for a time period of 60 s. Tables 2 and 3 summarize the main computational data of the four cases considered in the CPFD-Barracuda simulations. Note that the computational cost in the most restrictive case (Case 4) is approximately 30 h for 60 s of real time operation, i.e., approximately 0.5 h of computing time for 1 s of real time fluidization. The numerical simulations were performed in parallel using Intel Xeon CPU E5-2620 v4 @2.10 GHz (2 sockets and 8 cores per socket) with 64 GB RAM memory and the option for CUDA computing was enabled, with a Nvidia RTX A6000 graphics card.

In the CPFD-Barracuda simulations performed, absolute pressure and void fraction were obtained. To this end, several points placed at different heights along the bed and for different radial positions were defined along the computational domain, so some of these points were located in the same place as the experimental and numerical simulation carried out by Acosta-Iborra et al. [12].

**Table 2**
Cell and computational parameters for the different cases studied in the CPFD-Barracuda simulations: total number of cells $N_{cells,total}$, real number of cells $N_{cells,real}$, computational time $t_{comp.}$, *CFL* factor and number of time iterations $N_{iter}$.

| | $\Delta t$ [s] | $N_{cells,total}$ | $N_{cells,real}$ | $t_{comp.}$ [s] | *CFL* | $N_{iter}$ |
|---|---|---|---|---|---|---|
| Case 1 | $10^{-3}$ | 45980 | 38760 | $1.56 \times 10^4$ | 0.8–1.5 | $7.58 \times 10^4$ |
| Case 2 | | 93296 | 77112 | $2.69 \times 10^4$ | 0.8–1.5 | $1.11 \times 10^5$ |
| Case 3 | $10^{-4}$ | 45980 | 38760 | $7.62 \times 10^4$ | 0.1–0.4 | $6.01 \times 10^5$ |
| Case 4 | | 93296 | 77112 | $1.06 \times 10^5$ | 0.1–0.4 | $6.01 \times 10^5$ |
| Case 4a | $10^{-5}$ | 93296 | 77112 | $5.86 \times 10^5$ | 0.01–0.04 | $5.91 \times 10^6$ |
| Case 4b | $10^{-4}$ | 149193 | 121245 | $1.07 \times 10^5$ | 0.1–0.4 | $6.01 \times 10^5$ |

**Table 3**
Particle and mass parameters for the different cases studied in the CPFD-Barracuda simulations: Number of particles $N_{part.}$, number of clouds $N_{clouds}$, total mass of simulated particles, initial particle volume fraction $\theta_p$ and deviation in the mass $e_{mass}[\%]$.

| | $\Delta t$ [s] | $N_{part.}$ | $N_{clouds}$ | $m_{sim}$ [kg] | $\theta_p$ | $e_{mass}[\%]$ |
|---|---|---|---|---|---|---|
| Case 1 | $10^{-3}$ | $4.24 \times 10^7$ | $4.23 \times 10^5$ | 9.211 | 0.5437 | −1.15 |
| Case 2 | | $4.30 \times 10^7$ | $8.49 \times 10^5$ | 9.343 | 0.5514 | 0.259 |
| Case 3 | $10^{-4}$ | $4.24 \times 10^7$ | $4.23 \times 10^5$ | 9.211 | 0.5437 | −1.15 |
| Case 4 | | $4.30 \times 10^7$ | $8.49 \times 10^5$ | 9.343 | 0.5514 | 0.259 |
| Case 4a | $10^{-5}$ | $4.30 \times 10^7$ | $8.49 \times 10^5$ | 9.343 | 0.5514 | 0.259 |
| Case 4b | $10^{-4}$ | $4.30 \times 10^7$ | $1.34 \times 10^6$ | 9.343 | 0.5514 | 0.259 |

### 3.2.4. Sensitivity analysis of the cases studied

The influence of the time step and the grid size was studied through the four cases of the CPFD-Barracuda simulations. Firstly, the Courant-Friedrichs-Lewy (*CFL*) number is shown in Fig. 3, which is useful to determine the adequate time step based on the simulated meshes and parcels [23]. The software CPFD-Barracuda recommends a *CFL* value of between 0.8 and 1.5 to maintain a compromise between stability, accuracy, and speed of the calculation. If, during the simulations, the *CFL* reaches a value higher than 1.5, CPFD-Barracuda automatically reduces the time step for getting $CFL = 0.8$. For the cases with the highest time step (Cases 1 and 2), the software maintained the *CFL* factor between the default limits, reducing the time step when $CFL > 1.5$. In contrast, for Cases 3 and 4, with the lowest time step ($10^{-4}$ s), the *CFL* was not modified by the software during the simulations because it was under the maximum limit of $CFL = 1.5$, ranging between 0.1 and 0.4. The *CFL* behaviour helps to explain why the number of temporal iterations in Case 2 is higher than in Case 1, with the same time step. Case 2 had a lower cell size, so the *CFL* was higher and was corrected more times and, consequently, more iterations in time were needed. Regarding Cases 3 and 4, the number of iterations remained constant because no *CFL* correction was performed, so the difference in the computational time is only related to the different number of cells. Although *CFL* showed low values in the cases with the reduced time step, the highest computational cost (Case 4) showed a reasonable duration (Table 2). In addition to the four main cases studied, two extra cases (Cases 4a and 4b) were studied to check the independence of the numerical model from the time step and the number of cells. The only differences with respect to Case 4 is that in Case 4a the time step was reduced to $10^{-5}$ s, with the rest of parameters unchanged, whereas in Case 4b, the time step was the same as in Case 4 but the number of computational cells was augmented up to 149000. *CFL* data for Case 4a are very low, and the computational cost of this case is very high. Case 4b, shows similar values of the *CFL* to Case 4 with also a higher computational cost.

Table 3 includes the total number of real particles and clouds or clusters (a group of particles with the same properties) for each

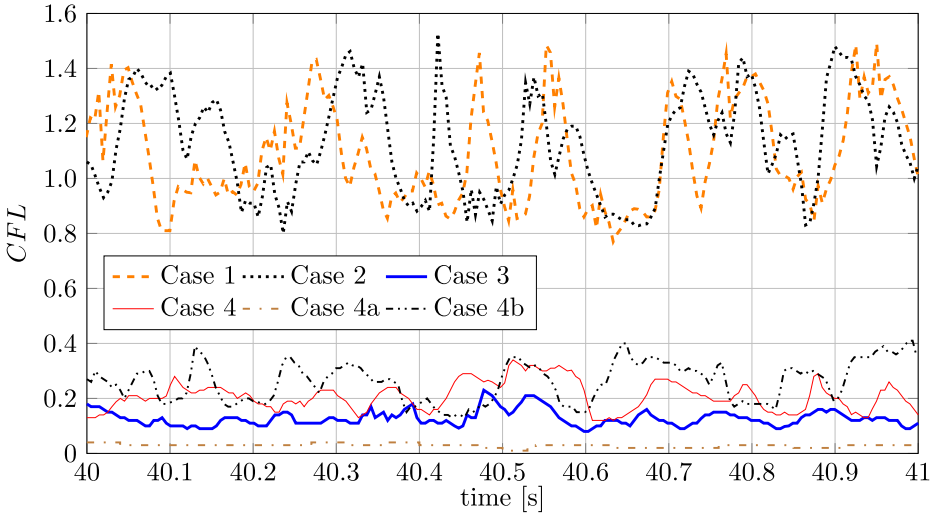


**Fig. 3.** Evolution of *CFL* factor for the four cases studied with CPFD-Barracuda.

case, which shows that the number of clouds increased proportionally to the number of computational cells, as expected. This table also includes the simulated mass of particles, which differs slightly from the theoretical mass imposed as the initial condition. This was reported by Liang et al. [23], who indicated that the change in the initial total solid mass is related to the way in which parcels are arranged in every cell, which depends on the cell shape and dimension. In this regard, CPFD-Barracuda maintains the height of the bed but modifies the mass in the bed, and consequently the initial particle fraction, to accommodate the total number of computational clouds in a rectangular array, that is, uniform in the three dimensions (the particles are initially located forming a regular hexahedron). Following this, the error in the initial mass ($e_{\text{mass}}$) was computed (Eq. (14)), resulting in a low value in all the analysed cases. Liang et al. [23] observed much higher values of $e_{\text{mass}}$, i.e. up to 15–20%, due to their 2-D numerical scheme with only one cell in the third dimension. This geometry limitation generated large mass variations to maintain the height of the bed.

$$e_{\text{mass}} = \frac{m_{sim} - m_{theo}}{m_{theo}} \times 100 \tag{14}$$

In Eq. (14), $m_{sim}$ is the simulated initial particle mass and $m_{theo}$ is the theoretical initial particle mass.

The mean manometric pressure during the 60 s of the simulations and the power spectral density (*PSD*) of pressure measurements are shown in Figs. 4 and 5, respectively. Fig. 4(a) shows the mean manometric pressure during the 60 s of the simulations. The first 2 s of each simulation were discarded due to the transient

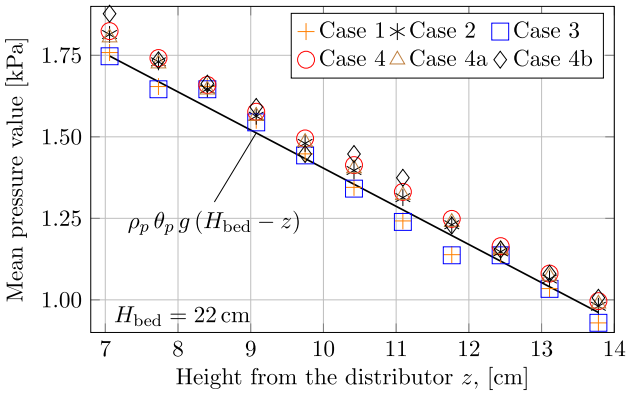


(a) Mean value

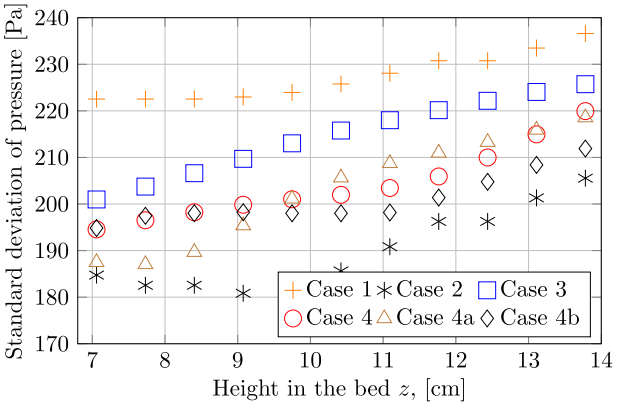


(b) Standard deviation

**Fig. 4.** Mean values of the manometric pressure (with $\theta_p = 0.45$) (a) and standard deviation (b) of pressure signal for different heights in the centre of the bed for the four cases studied with CPFD-Barracuda.

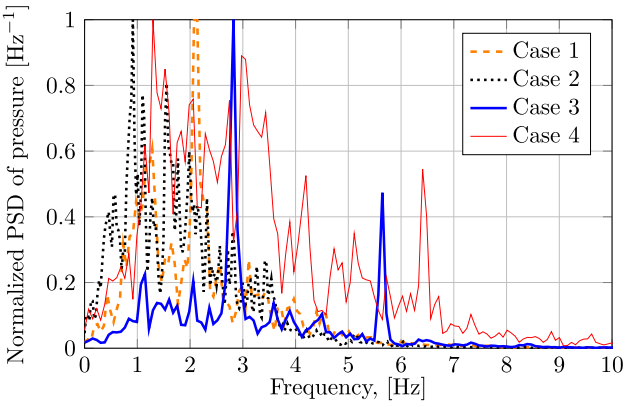


(a) $z = 7$ cm

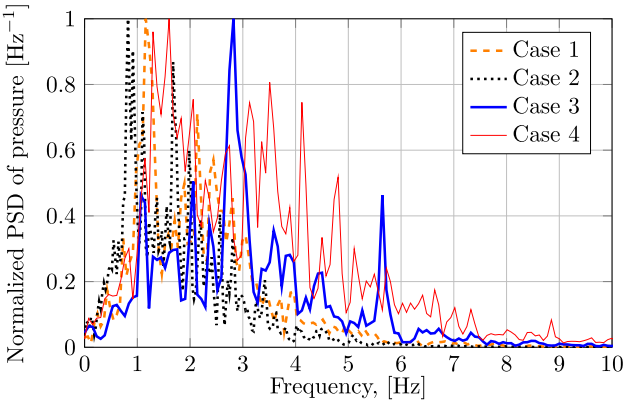


(b) $z = 13$ cm

**Fig. 5.** Comparison of normalized power spectral densities (*PSD*) for absolute pressure at z = 7 cm (a) and z = 13 cm (b), in the bed axis for the different cases studied with CPFD-Barracuda.

start-up of the bed. There are no noticeable differences between the analysed cases. In Fig. 4(a) the theoretical line was calculated with a value of $\theta_p = 0.45$, which was the mean value computed in the simulations. It is observed that the theoretical value properly fits with the computed data with small differences between the different cases. Note that the mean pressure value is similar in the cases with an equal number of cells (Cases 1 and 3 and Cases 2 and 4), in which the mass of particles is also the same (see Table 3). Fig. 4(b) shows the standard deviation of the pressure measurements. It can be observed that, for a fixed time step, the standard deviation decreases when the number of computational cells increases. These differences are larger in the case of the largest time step ($10^{-3}$ s). The reduction in the standard deviation could be related with an increase in the bubble size with a coarser mesh. With a lower spatial resolution, the fraction of particles within a bubble is higher, and this provokes that the bubbles growth in size for the same excess air flow over minimum fluidization conditions.

To check the independence of the numerical results from the time step and the mesh, the data for Cases 4a and 4b are also plotted in Fig. 4(b). It can be observed that the standard deviation of the pressure fluctuation in Cases 4a and 4b are similar to the values obtained in Case 4. Thus, reducing the numerical time step below $10^4$ s and increasing the number of cells over $10^5$ elements did not improve the numerical results but augmented the computational cost. Regarding the time step influence, when comparing Case 4a and Case 4, the maximum discrepancy between the

standard deviation of pressure was 2.3% (at $H_{bed} = 8$ cm), whereas the computational cost at Case 4a was approximately 450 % higher than Case 4. Regarding the influence of the grid size, when comparing Case 4b and Case 4, the standard deviation of pressure was similar, obtaining maximum discrepancies close to 1.8%.

Fig. 5 shows the *PSD* of pressure measurements at two different heights in the bed ($z = 7$ cm and $z = 13$ cm). The procedure to obtain the PSD is similar to that reported in [12], and is described in more detail in Section 4.1. In general, it can be observed that Cases 1 and 2 present one dominant peak in the spectrum, whereas Cases 3 and 4 present peaks with more energy for frequencies over 2.5 Hz. In general, for frequencies higher than 3 Hz, Case 4 shows larger peaks, which are not detected in the other cases, except a large peak detected in Case 3 at 5.75 Hz for both heights. The high peaks observed in the Case 4 at large frequencies could be related with the combination of a small mesh size and time step of this case. The small mesh size may not filter the perturbations propagation, as occurs in higher mesh sizes, and the small time step could detect the high frequency fluctuations of the pressure, which are not observed or mitigated with a higher time step.

Fig. 6 compares the bubble frequency along the height of the bed for two different radial positions, at the central axis of the bed (Fig. 6a) and Fig. 6)) and at a radial position of $0.8R$ (Fig. 6b) and Fig. 6(d)). This bubble frequency was calculated considering that a bubble is passing at a given point if the particle volume fraction at this point falls below a threshold value. Figs. 6(a) and 6(b) show the data obtained for a threshold (*th*) in the particle fraction obtained as the mean value at each point, $th = \bar{\theta}_p$, and Figs. 6(c) and 6(d) with a value of *th* of 0.3. The mean value $\bar{\theta}_p$ was calculated as the mean value over the 58 s of the simulations, as the two first seconds were discarded, resulting in $\bar{\theta}_p \approx 0.5$. The *th* value selected to detect bubbles in fluidized beds varies in the literature. Acosta-Iborra et al. [12] performed a sensibility analysis of the *th* value for the same case studied in this work and observed that the number of bubbles and the chord lengths decreased when *th* decreases. They finally assumed $th = \bar{\theta}_p$, which has the advantage of being adaptive for each bed regime. Other works [36,38] used $th = 0.3$. There are no great differences between the four cases. Only in Fig. 6(b) can it be clearly observed that Cases 3 and 4 (with the

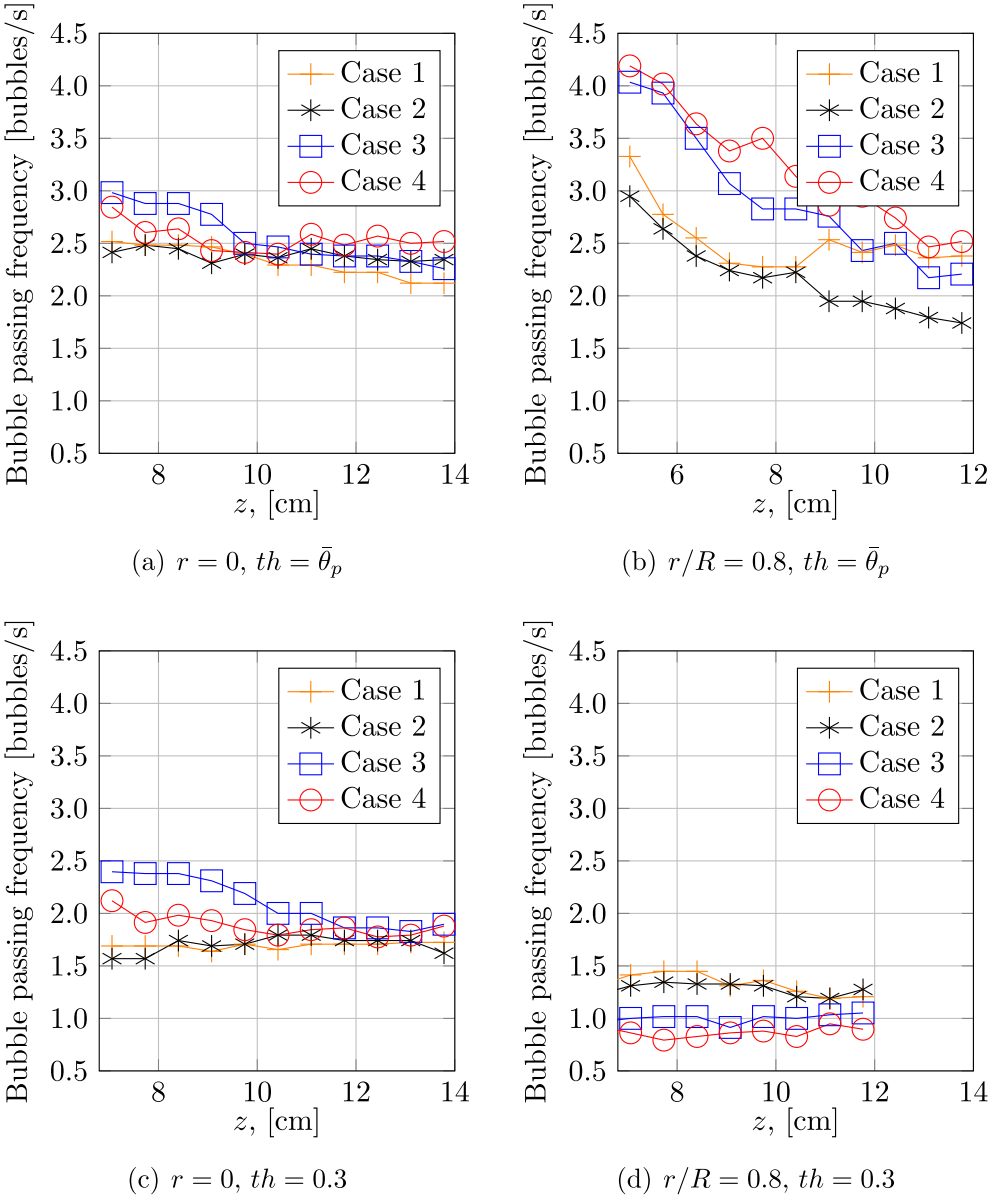


**Fig. 6.** Comparison of bubble frequency at different radial positions $r = 0$ and $r = 0.8R$ for two different values of the threshold of the particle fraction used to detect the bubbles in the CPFD-Barracuda simulations.

lowest time step, $10^{-4}$ s) predict higher bubble frequency, especially close to the bed bottom. With a $th = 0.3$, the bubble frequency is always smaller in comparison with the bubble frequencies obtained with the mean $th = \bar{\theta}_p \approx 0.5$, especially for the case at $r = 0.8R$. These results coincide with the numerical results of Acosta-Iborra et al. [12], as the number of bubbles detected increases when *th* is augmented. In the four cases studied, the bubble frequency decreases along the bed height due to the bubble coalescence, so at higher heights in the bed the number of bubbles is reduced and their size increases.

In accordance with the aforementioned results, Case 4 was selected in the comparison analysis of the CPFD-Barracuda results with the main experimental and the numerical results obtained by Acosta-Iborra et al. [12]. For the cases with the lowest time step (Cases 3 and 4), more frequency peaks were detected. Moreover, Cases 1 and 2 were discarded because they detected peaks of energy for frequencies slightly different to the other cases. It is worth noting that Cases 3 and 4 showed similar results for the frequencies of the spectrum and bubble frequency, although Case 4 detected peaks at frequencies higher than 5.75 Hz and showed less $e_{\text{mass}}$ (-1.15% for Case 3 and 0.26% for Case 4). Moreover, although the number of computational cells in Case 4 was approximately 100% higher than in Case 3, the computational cost was not exceptionally high, thus finding this case adequate to show accurate results. Cases 4a and 4b are discarded due to their higher computational cost without improving the accuracy of the results.

## 4. Results

Fig. 7 shows snapshots of the evolution of the particle volume fraction in the bed over 0.9 s starting from $t = 10$ s. The snapshots clearly show different bubbles (regions of low particle concentration) ascending along the bed height and erupting at the bed surface. At $t = 10$ s, close to the bed surface, there is a chain of bubbles, which erupt at the bed surface at $t = 10.1$ s. The bubble eruption causes a large projection of particles over the free surface, which are clearly observed from $t = 10.2$ s up to $t = 10.4$ s. When two or more bubbles coalesce at the bed surface, the velocity of the projected particles are notably increased [43]. They are projected either from the dome of the leading bubble or from the wake of the trailing bubble. A similar behaviour is observed in the second half of the period, between $t = 10.5$ s and $t = 10.9$ s. a chain of bubbles ascends and coalesces until reaching the bed surface, where it projects the solids.

### 4.1. Frequency analysis

Figs. 8 and 9 show, respectively, the time evolution of the pressure fluctuations and the particle fraction (or, equivalently, the optical signal) obtained at $r/R = 0.8$ and $z = 12$ cm. Both figures show the experimental (black solid line) and numerical results carried out with TFM-Fluent by Acosta-Iborra et al. [12] (red dotted line) and the ones obtained in this work with CPFD-Barracuda (blue shaded line). In particular, Fig. 8 shows the pressure fluctuations over the mean pressure, i.e. $p - \bar{p}$, and it can be clearly observed that the amplitude of the experimental values are much higher than that of the two numerical models. In the experimental data, there are fluctuations up to 1 kPa, whereas in the numerical simulations these fluctuations are less than 0.5 kPa. Fig. 9(a) shows the signal in volts acquired using optical probes which is related to the local particle fraction in the bed at the measurement point. When a bubble passes in front of the probe the reflected light is lower than the reflected light by the emulsion phase (high concentration of particles) and the voltage falls rapidly [44]. Separately, due to the scale difference, Fig. 9(b) represents the time evolution of the solid fraction $\theta_p$ obtained at the same sampling point with TFM-Fluent and CPFD-Barracuda. A qualitative comparison indicates that experimental measurements detect more fluctuations of high frequency than the numerical simulations. These fluctuations are related to the random noise present in any experimental measurement. The particle fraction in both the TFM-Fluent and the CPFD-Barracuda simulations are practically invariable, with a value of approximately 0.54, excepting when a bubble pierces the sampling point, which is clearly observed as a large reduction in $\theta_p$.

The *PSD* of the absolute and differential pressure measurements and local particle volume fraction were obtained to analyse the bed dynamics. The sub-spectral densities of data were averaged to reduce their variance [45,12]. The analysis of the numerical results obtained from CPFD-Barracuda were pre-processed following the methodology proposed by Acosta-Iborra et al. [12]. More specifically, the *PSD* were obtained with the average spectrum from eight consecutive sections of the signal with 50% overlapping and a Hamming window to smooth the signal at the section endpoints.

Fig. 10 compares the results of the normalized *PSD* obtained from absolute (i.e. manometric) and differential pressure signals reported by Acosta-Iborra et al. [12] from experimental data and from TFM-Fluent numerical simulations, together with the new values obtained with CPFD-Barracuda. Note that the absolute pressure data are representative of the global behaviour of the bed, which is primarily affected by the level fluctuations of the bed surface due to bubble bursting. In contrast, the signal of a pressure difference is indicative of the bubble passing frequency at a given point, which is representative of the local bed dynamics at that point.

Figs. 10(a) and 10(b) show the global behaviour of the bed by means of the *PSD* obtained from the absolute pressure data at two different heights from the distributor: $z = 7$ cm and $z = 12$ cm. On first glance, at $z = 12$ cm, the *PSD* from absolute pressure signals obtained with CPFD-Barracuda contains the largest peaks of the spectrum at low frequencies (below 2 Hz), which is not observed in both the experimental results and the TFM-Fluent simulation. These low frequency peaks of the CPFD-Barracuda results are also observed in the *PSD* obtained at $z = 7$ cm (Fig. 10(a)). However, the low frequency peaks do not appear in the *PSD* of the differential pressure signals from the CPFD-Barracuda simulation, as shown in Fig. 10(c) at $z = 12.5$ cm. This differential pressure signal was calculated as the difference between the absolute pressure signal at $z = 13.0$ and 12.0 cm. A similar behaviour is observed with TFM, as the dominant frequency for absolute pressure signals (Figs. 10(a) and 10(b)) is lower than the predicted from differential pressure data (Fig. 10(c)). This fact suggests that these low frequency peaks could be related to the level oscillations of the free surface of the bed, which are observed in the PSD of absolute pressure signal with CPFD-Barracuda and TFM-Fluent, but not in the differential pressure signal. In addition, the bubble frequency in the center of the bed at $z = 7$ cm (Fig. 10)) and $z = 12$ cm (Fig. 10(b)) in CPFD-Barracuda is 2.5 Hz, whereas it is 4.4 Hz for TFM-Fluent. The higher bubble frequency (and consequently larger number of bubbles erupting at the bed surface) in TFM-Fluent is in concordance with the higher frequencies observed in Figs. 10(a) and 10(b).

Table 4 summarizes the main frequencies of the *PSD* observed in Fig. 10 at $z = 12$ cm. The main peak of the *PSD* obtained from the experimental signal of absolute pressure is 2.7 Hz, slightly different to the natural frequency of the bed, 2.1 Hz, as shown in Acosta-Iborra et al. [12]. The results from CPFD-Barracuda at $z = 12$ cm have a frequency peak at 3.1 Hz, which is quite close to the 2.7 Hz peak of the experiments. However, as mentioned before, the *PSD* of the absolute pressure from the CPFD-Barracuda also shows a main peak at lower frequencies (i.e.

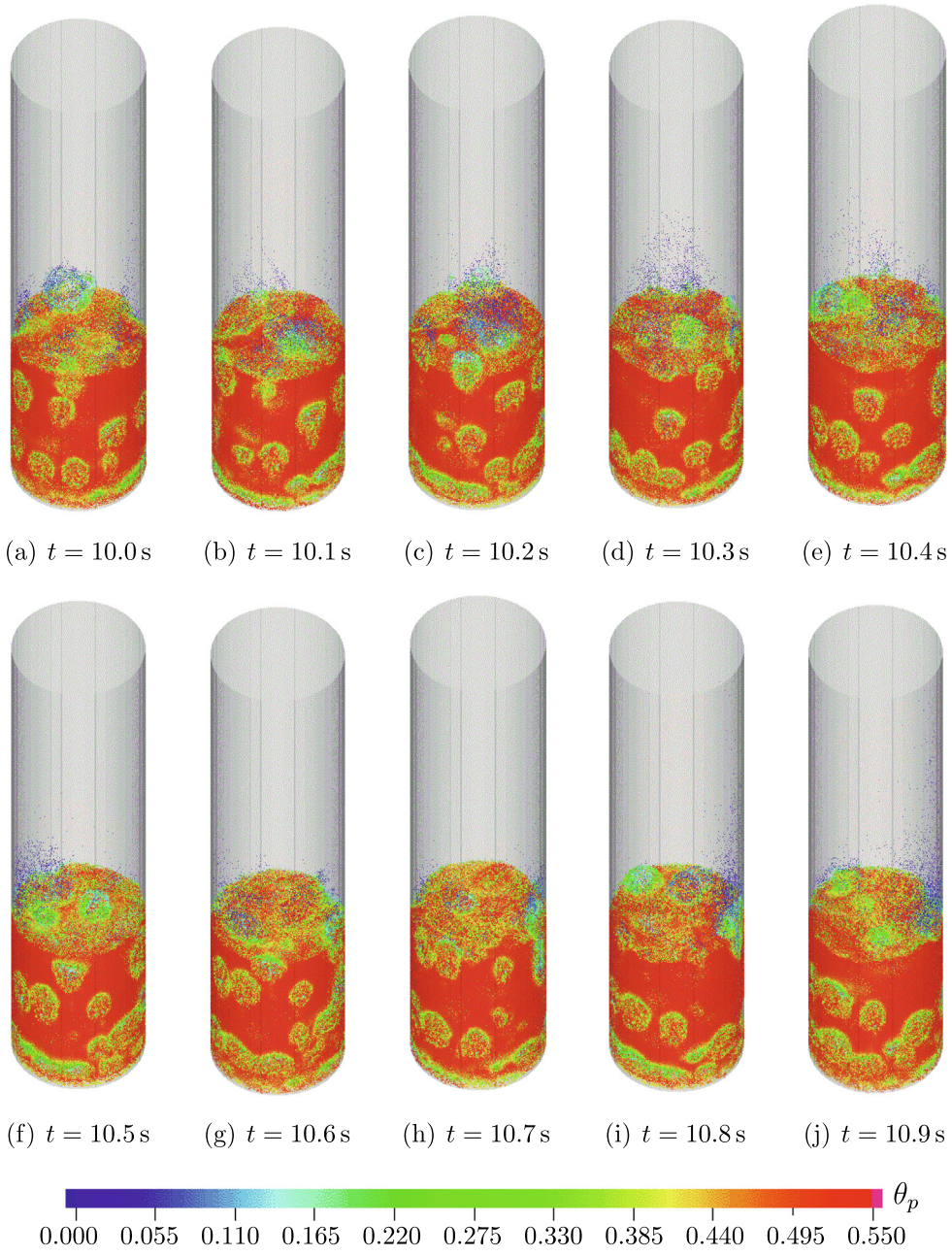


**Fig. 7.** Snapshots of particle volume fraction $\theta_p$ evolution between $t = 10.0$ s and $t = 10.9$ s obtained with CPFD-Barracuda.

1.3 Hz). This main frequency is close to the experimental result. The TFM-Fluent simulation yields a main frequency of the absolute pressure of 3.4 Hz, which is slightly higher than that from CPFD-Barracuda. These discrepancies could be related with the higher bubble frequency predicted by TFM-Fluent, as commented in the previous paragraph.

Figs. 10(c) and 10(d) show the *PSD* obtained from differential pressure and particle volume fraction, respectively. In both cases, the *PSD* obtained with CPFD-Barracuda has a very reduced contribution of frequencies over 7 Hz, compared to that in the experiment and the TFM-Fluent spectra. This is arguably due to the way CPFD-Barracuda obtains the particle volume fraction. As CPFD-Barracuda simulates discrete particles or clouds, this discrete information has to be spatially filtered to be transformed into a continuous field of particle volume fraction for each computing cell [46]. In particular, CPFD-Barracuda calculates the Particle Volume Fraction in an Eulerian cell using linear interpolation functions that takes into account the cells adjacent to the location of the computational particle or cluster [20]. This transformation could reduce the high frequencies in the resulting *PSD* of particle volume fraction.

The main frequencies of the differential pressure spectrum and the particle volume fraction (or optical signal) spectrum are listed in Table 4. The first frequency peak $f_{dif,1}$ in terms of intensity in the *PSD* of differential pressure, excluding the frequency peaks coincident to those of the absolute pressure spectrum, appears at 6.3 Hz in the experiments and at 6.1 Hz in the TFM-Fluent simulation. In the CPFD-Barracuda simulation, $f_{dif,1}$ is located at the lower, but relatively close, frequency of 4.8 Hz. As expected, the results for the frequency peak with the second largest intensity, $f_{dif,2}$, are

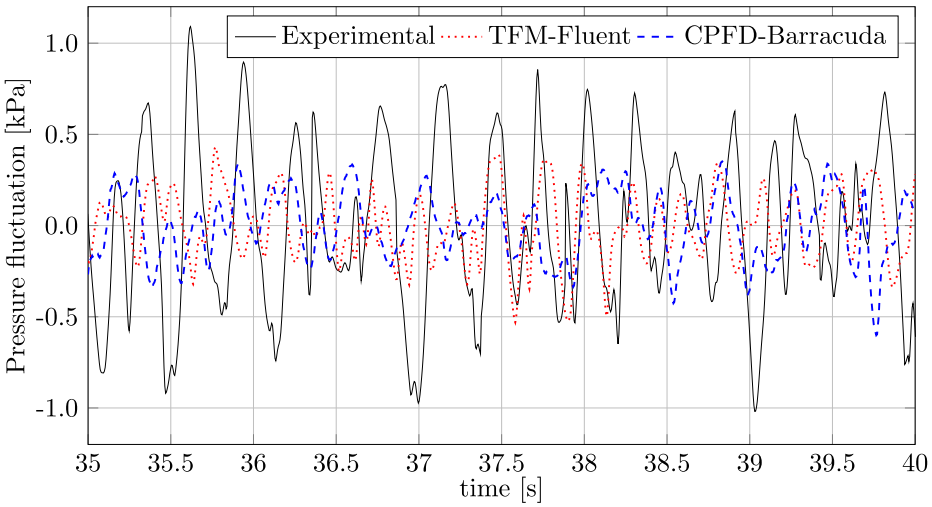


**Fig. 8.** Pressure fluctuation over the mean value $(p - \bar{p})$ during 5 s at $z = 12$ cm and $r/R = 0.8$.

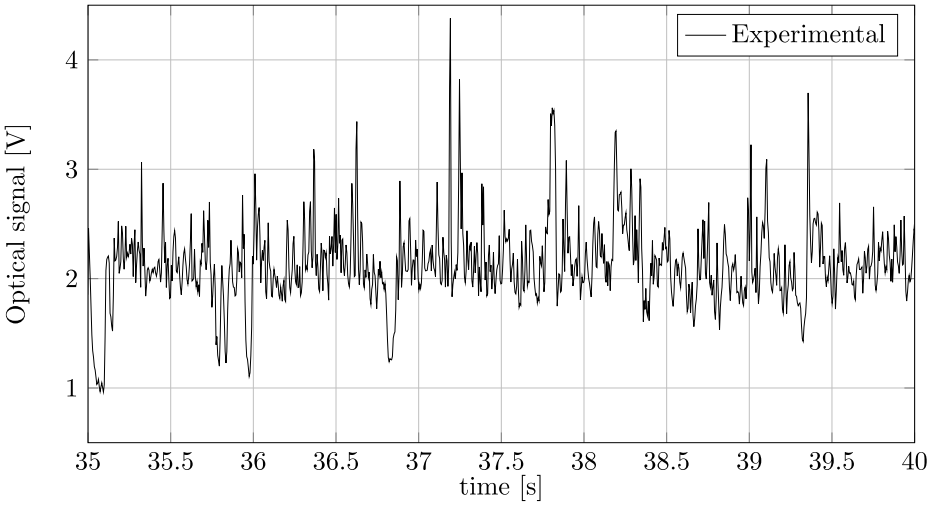


(a) Experimental optical signal

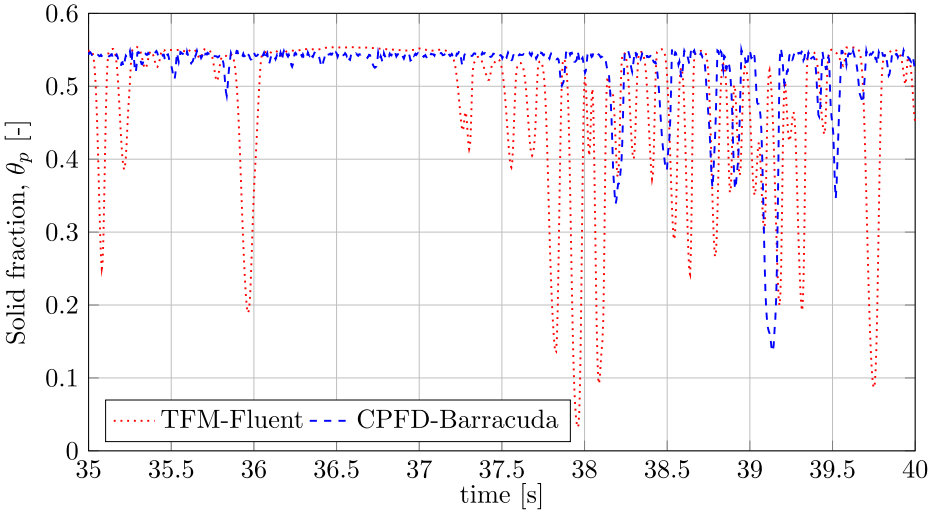


(b) Numerical solid fraction

**Fig. 9.** Optical signal experimentally measured [12] during 5 s (a) and solid fraction numerically obtained (b) at $z = 12$ cm and $r/R = 0.8$.

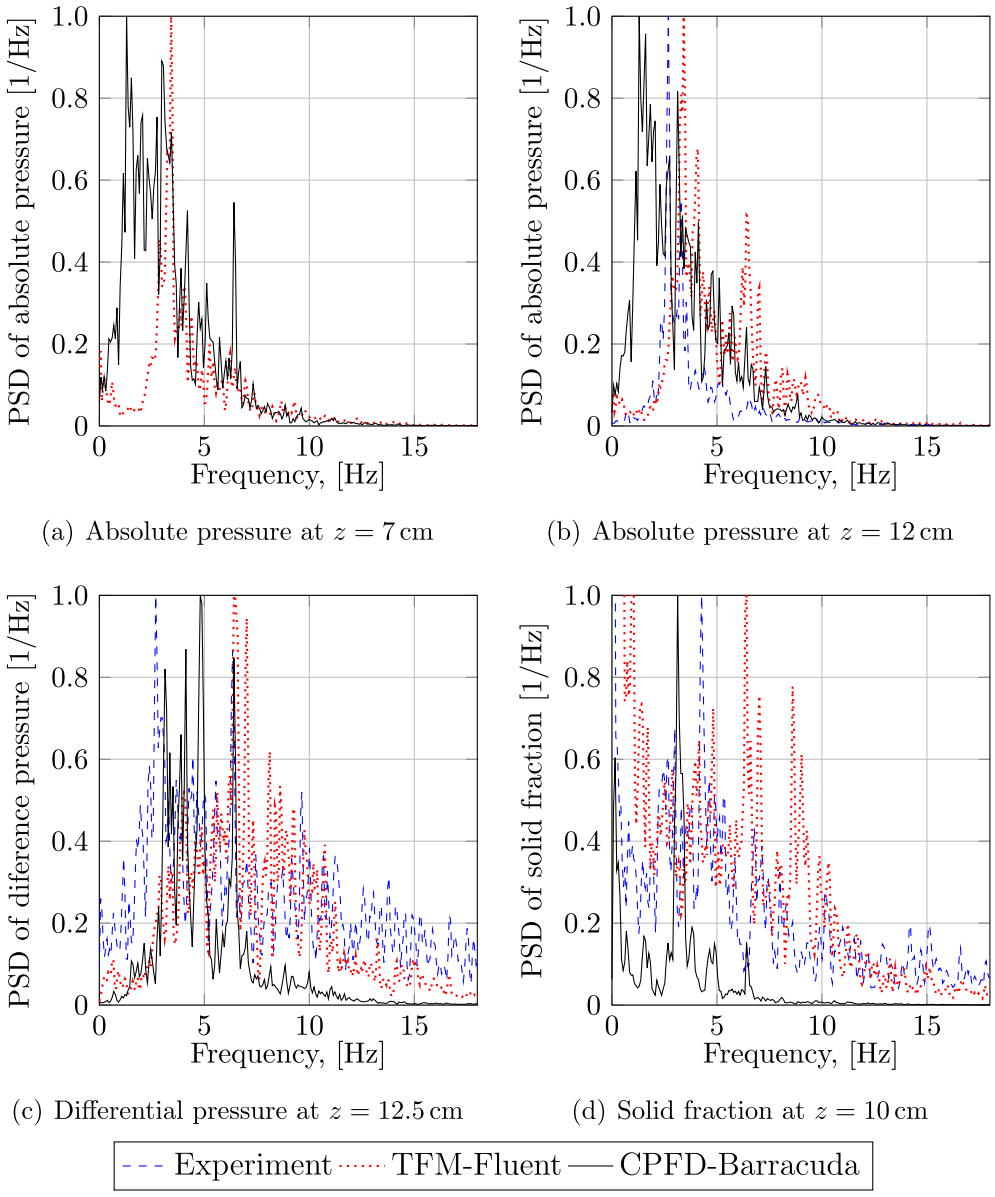


**Fig. 10.** Normalized *PSD* obtained from experimental results [12] (dashed blue lines), from TFM Fluent [12] (dotted red lines) and from CPFD-Barracuda (solid black lines). Figures (a) and (b) show the data obtained from absolute pressure at $z = 7$ and $z = 12$ cm, respectively, Figure (c) the data obtained from differential pressure at $z = 12.5$ cm and Figure (d) the data obtained from particle fraction at $z = 10$ cm. All the data were obtained in the centre of the bed ($r/R = 0$).

**Table 4**
Main peaks obtained from the different *PSD* shown in Fig. 10.

| | Experiments | TFM-Fluent | CPFD-Barracuda |
|---|---|---|---|
| Absolute pressure | | | |
| $f_d$ [Hz] | 2.7 | 3.4 | 3.1 |
| Differential pressure | | | |
| $f_{dif,1}$ [Hz] | 6.3 | 6.5 | 4.8 |
| $f_{dif,2}$ [Hz] | 4.5 | 8.1 | 6.4 |
| Optical signal or particle volume fraction | | | |
| $f_{opt,1}$ [Hz] | 6.8 | 6.4 | 3.1 |
| $f_{opt,2}$ [Hz] | 4.3 | 8.0 | 1.5 |

more scattered. While the differential pressure signal from the experiment yields $f_{dif,2} = 4.5$ Hz, this value is $f_{dif,2} = 6.4$ Hz in the CPFD-Barracuda simulations and reaches $f_{dif,2} = 8.1$ Hz in the case of the TFM-Fluent simulation. An analogous situation occurs for the particle volume fraction, as shown in Table 4. The first peak of the spectrum of the particle volume fraction $f_{opt,1}$ obtained from the CPFD-Barracuda simulation is 3.1 Hz, which is nearly half that from the experimental optical signal (6.8 Hz) and from the particle volume fraction simulated with TFM-Fluent (6.4 Hz). In the CPFD-Barracuda simulation, $f_{opt,1}$ is nearly 40% smaller than $f_{dif,1}$, and this difference is higher than in the experimental and TFM model results. This also happens with the second peak of the particle volume spectrum, $f_{opt,2}$. The CPFD-Barracuda simulation leads to $f_{opt,2} = 1.5$ Hz, which is much smaller than $f_{diff,2}$ obtained from the same code. This reinforces the hypothesis of high frequency filtering in the particle volume fraction results and the lower bubble frequency from CPFD-Barracuda.

### 4.2. Bubble characteristics: pierced length, velocity and frequency

Bubble pierced length, velocity and frequency were calculated from the simulation particle fraction signal and from the optical probe experimental signal. For the detection of bubbles using the

optical probes, when the voltage signal falls below a threshold value, a bubble passage is considered to be occurring. The threshold value was determined by plotting the histogram of the voltage output signal of the optical probes. The histogram exhibits a peak corresponding to the dense phase and a tail corresponding to the gas bubble phase. The bubble detection threshold was defined as the voltage where the histogram tail begins and the slope of the histogram becomes nearly zero. A more detailed explanation can be found in Sobrino et al. [44]. For both simulated and experimental signals, bubble velocity can be calculated dividing the vertical distance between two consecutive virtual or experimental probes by the time the bubble takes to travel from the lower to the upper probe. The bubble pierced length is then calculated by multiplying the bubble rise velocity by the bubble passage time. The bubble passage time is the period during which the particle volume fraction signal or the optical probe signal falls below a given threshold. Further details on the determination of bubble characteristics can be found in [12].

Fig. 11(a) shows the mean pierced length ($\bar{y}$) and the mean bubble velocity ($u_b$) measured at height of $z = 7.5$ cm for different radial positions in the bed. The results are presented for two threshold values for bubble detection: $\bar{\theta}_p$ and 0.3. It can be clearly observed that for $th = 0.3$ the pierced lengths are smaller than for $th = \bar{\theta}_p$, as expected. Nevertheless, the variations in $\bar{y}$ with the threshold value are higher in the TFM-Fluent simulations, with a reduction of approximately 1 cm (from 4 to 3 cm), whereas the reduction in CPFD-Barracuda is 0.3 cm, approximately. These

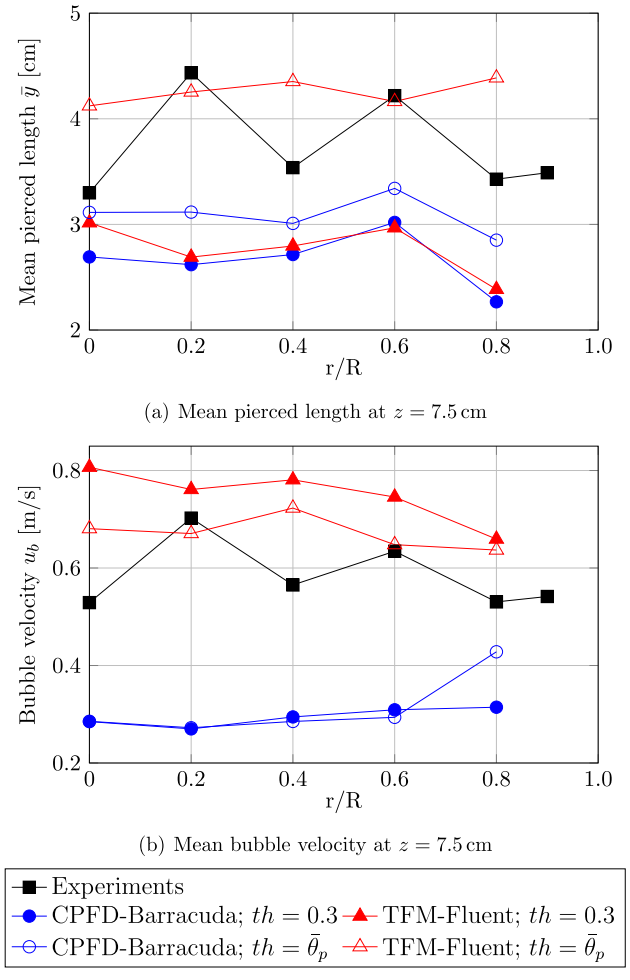


(a) Mean pierced length at $z = 7.5$ cm

(b) Mean bubble velocity at $z = 7.5$ cm

**Fig. 11.** Time averaged pierced length (a) and bubble velocity (b) for different radial positions in the bed at $z = 7.5$ cm.

results indicate that CPFD-Barracuda is less sensitive to the threshold value than TFM-Fluent. Regarding bubble velocity (Fig. 11(b)), the CFPD-Barracuda results are not influenced by the threshold value, except for the region close to the bed wall ($r/R = 0.8$), while in TFM-Fluent, the bubble velocity varied slightly with the threshold (approximately 0.1 m/s). In view of this figure, the arbitrary threshold value selected to define bubble contour in TFM-Fluent can notably influence on the results. As TFM-Fluent models the system as two interpenetrating fluids, the selection of the bubble threshold defines the limit between the bubble and the dense phase. In contrast, CPFD-Barracuda has the advantage of modeling the motion of groups of particles, and consequently, the numerical results are much less dependent of the selection of an arbitrary threshold value. The transition from the dense to the bubble phase in the TFM is by nature smoother than the lagrangian perspective of CPFD-Barracuda. Nevertheless, in the procedure to calculate Particle Volume Fraction with CPFD-Barracuda, it is obtained using linear interpolations factors that takes into account the computational cells adjacent to the location of the computational particle. This fact may smooth also the results. Another important factor that may explain the differences in the threshold sensibility is the differences in the cell size, which are smaller in CPFD-Barracuda (93296 cells) than in TFM-Fluent (28800 cells). A lower number of cells provokes larger spatial variations in the bubble contour detection when the threshold value is varied.

Fig. 11 shows that in the region closer to the wall ($r/R = 0.8$) CPFD-Barracuda predicts higher bubble velocities when $th = \bar{\theta}_p$ is used. This fact is related with the change in the threshold value calculated for this case. For values of $r/R \lesssim 0.6$, $\bar{\theta}_p \approx 0.55$, whereas at $r/R = 0.8$ this value is reduced to $\bar{\theta}_p = 0.49$. The lower value of the average in time particle volume fraction is related with a preferential bubble path in this zone [47]. TFM-Fluent does not predicts an increase of the bubble velocity close to the wall, which could be related with the differences in the boundary conditions in both models. As it is explained in Fig. 1, TFM-Fluent imposes a free-slip condition for the particles, whereas CPFD-Barracuda uses a coefficient for the normal and tangent momentum retention and diffuse bounce when the particles are in contact with the wall.

According to the results showed in Fig. 11 CPFD-Barracuda underestimates the experimental results for bubble pierced lengths and velocities. These differences could be related with the drag model used in CPFD-Barracuda. Pal and Theuerkauf [48] adjusted the model multiplier of Wen-Yu model to make the model more suitable for close packing. These authors observed that there are different optimum coefficients, depending on the particle size and density. TFM-Fluent used Gidaspow drag model. The differences between both models could explain the lower values predicted by CPFD-Barracuda in comparison with TFM-Fluent.

Compared with experimental data obtained with optical probes, CPFD-Barracuda, regardless of the threshold value, predicts smaller bubble lengths with smaller bubble velocities. The TFM-Fluent results obtained with the mean threshold are closer to the experiments, but TFM-Fluent is highly influenced by the threshold value selected to determine bubbles in the bed.

Fig. 12 also shows the mean pierced length, $\bar{y}$ and bubble velocity, $u_b$, along the height of the bed for a fixed radial position of $r/R = 0.8$. Comparing the results along the bed height, the conclusions are similar to Fig. 11: the mean pierced length obtained for TFM-Fluent is largely influenced by the threshold value and these variations are smaller in CPFD-Barracuda. Moreover, both models show the pierced length increase with the bed height (see Fig. 12 (a)). Regarding bubble velocity (Fig. 12(b)), it is less influenced by the threshold value in both numerical models. TFM-Fluent overpredicts the experimental data and predicts an increase in the bubble velocity along the bed height, as also observed for the

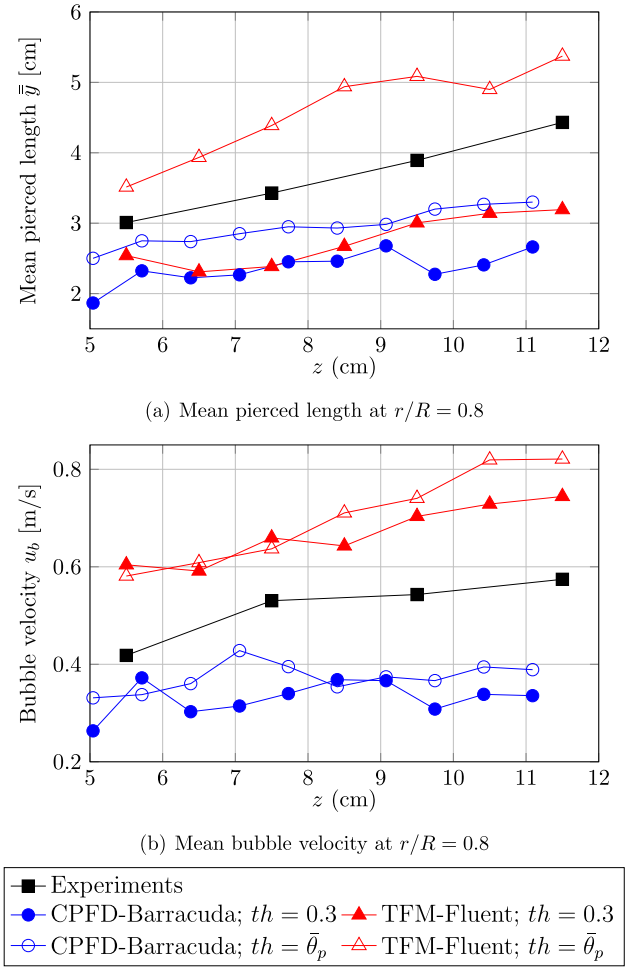


(a) Mean pierced length at $r/R = 0.8$

(b) Mean bubble velocity at $r/R = 0.8$

**Fig. 12.** Time averaged pierced length (a) and bubble velocity (b) for different heights in the bed at $r/R = 0.8$.

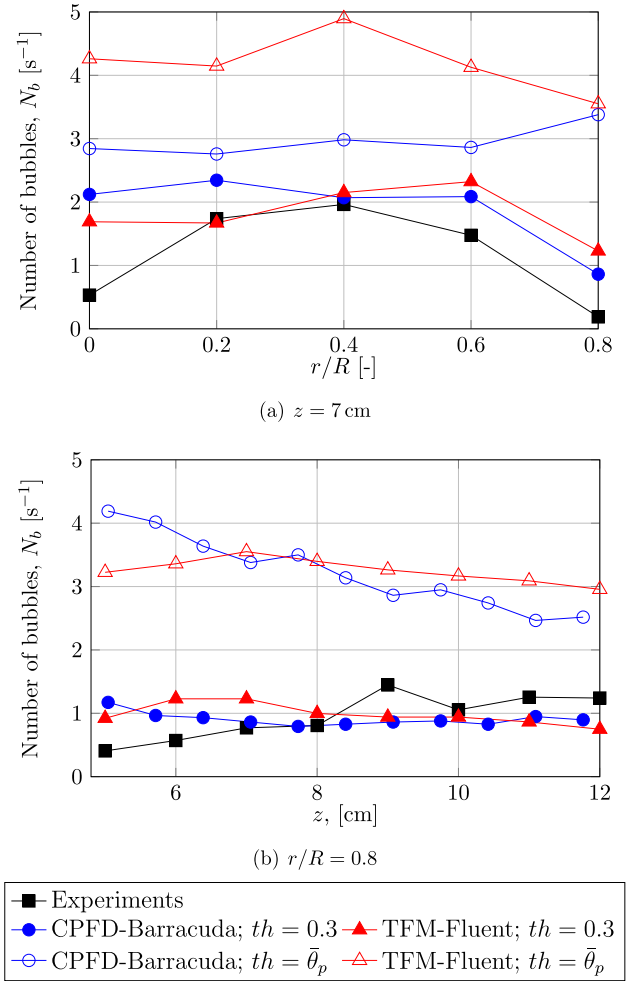


(a) $z = 7$ cm

(b) $r/R = 0.8$

**Fig. 13.** Number of bubble per second detected for different radial positions at $z = 7$ cm (a) and for different heights at $r/R = 0.8$ (b).

experiments, while CPFD-Barracuda obtains lower values and shows and almost constant bubble velocity with the bed height. A cause of these distinct behaviour in bubble velocity observed in the simulations can be the drag model employed in CPFD-Barracuda (Wen-Yu) and TFM-Fluent (Gidaspow).

Finally, the number of bubbles per second (bubble frequency) detected is shown in Fig. 13. Fig. 13(a) shows the radial variation at a height of $z = 7$ cm from the distributor and Fig. 13(b) shows the variation with height for a radial position $r/R = 0.8$, for the experimental and numerical results considering a threshold value calculated as the mean in each point and $th = 0.3$. In Fig. 13(b) the two numerical models present similar results for the same threshold value, although the numerical data obtained with the mean threshold tend to overestimate the experimental results. A threshold of $th = 0.3$ obtains numerical results closer to the experiments. Regarding the radial distribution (Fig. 13(a)), the experimental results indicate there are more bubbles in the region $0.2 < r/R < 0.6$ and fewer in the centre of the bed ($r/R = 0$) and close to the wall ($r/R = 0.8$). CPFD-Barracuda and TFM-Fluent also reduce the bubble frequency close to the bed wall, although they present a higher number of bubbles in the centre of the bed than in the experiments.

### 4.3. Equivalent volume bubble diameter

Fig. 14 shows the Probability Density Functions (*PDF*) for the pierced length, $y$, the volume equivalent bubble diameter $D_v$ and the bubble velocity $u_b$. The *PDFs* were obtained using the maximum entropy method [49,44]. This method has been used to obtain the *PDF* of $y$ and $u_b$ and a continuous distribution of the bubble size $D_v$ in a two-phase system from pierced lengths, assuming a bubble geometry. Santana et al. [49] applied this method to gas bubbles in water with an ellipsoidal geometry. Later, Sobrino et al. [44] extended this method for bubbling fluidized beds, assuming a truncated oblate ellipsoidal bubble and applied to both pressure and optical experimental signals. The reader is referred to these works for a detailed description and numerical implementation of the Maximum Entropy Method, which is beyond the scope of this work.

The *PDF* is presented for two heights ($z = 7.5$ cm and 9.5 cm) for a threshold $th = \bar{\theta}_p$ to determine the pierced lengths and bubble velocities in TFM-Fluent and CPFD-Barracuda. The shape of the PDFs obtained with $th = \bar{\theta}_p$ for TFM-Fluent and CPFD-Barracuda are similar to the experimental ones, although CPFD-Barracuda predicts slightly smaller pierced lengths and diameters and less wide distributions than the experiments. Overall, pierced length, diameter and bubble velocity distributions predicted by CPFD-Barracuda are smaller than the experimental and TFM-Fluent results.

Fig. 15 shows the mean value and the standard deviation of $D_v$ along the bed height for a radial position $r/R = 0.8$. The results are similar to those shown in Fig. 12(a) for pierced lengths, as the volume equivalent bubble diameter is inferred from pierced lengths. It

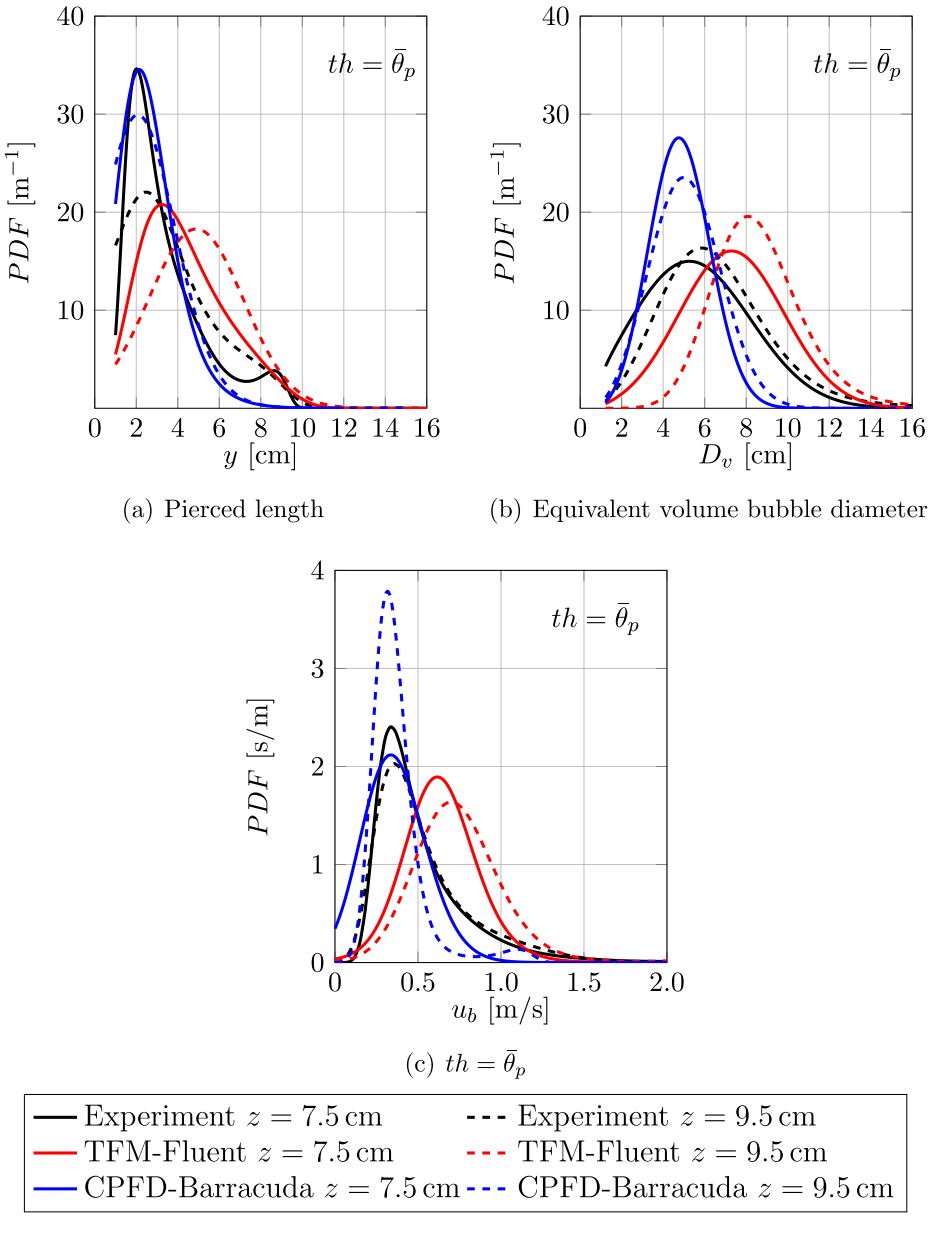


(a) Pierced length (b) Equivalent volume bubble diameter

(c) $th = \bar{\theta}_p$

**Fig. 14.** Probability density function of the pierced length (a), of the equivalent volume bubble diameter (b) and of the bubble velocity (c) at $r/R = 0.8$ for different heights.

can be observed that CPFD-Barracuda underpredicts the experimental bubble size, whereas TFM-Fluent overpredicts this value. The same figure shows the mean pierced lengths, $\bar{y}$ obtained from CPFD-Barracuda, for a threshold $th = \bar{\theta}_p$ and the correlation proposed by Agarwal [50], which is in close agreement with the CPFD-Barracuda results. Karimipour and Pugsley [51] and Rüdisüli et al. [52] reported that the mean value of the bubble equivalent diameter can be computed as 1.744 times the mean values of the pierced lengths. This is well in line with the Agarwal correlation and CPFD-Barracuda results.

The standard deviation of $D_v$ along the bed height is shown in Fig. 15(b). It can be observed that the CPFD-Barracuda results predict smaller standard deviation of the bubble size distribution than the experiments and TFM-Fluent, which both present similar values. However, the CPFD-Barracuda results show a monotonic increase in the standard deviation with height, which is also revealed in the experiments, while the standard deviation remains more approximately constant for TFM-Fluent simulation. As it was commented previously in Section 4.2, at $r/R = 0.8$ CPFD-Barracuda predicts a preferential path of the bubbles in the bottom of the bed ($z \lesssim 7$ cm), in which there is a chain of bubbles of similar sizes. This justifies the lower values of the standard deviation in this zone.

## 5. Conclusions

The analysis carried out in this work, comparing CPFD-Barracuda and TFM-Fluent simulations as well as experimental data, reveals that the threshold value of the particle fraction selected for detecting and demarcate bubble borders in fluidized beds notably affects the mean pierced length of the bubbles simulated by TFM-Fluent. However, the influence of the selected threshold in $\bar{y}$ is much smaller for CPFD-Barracuda simulations. The bubble frequency also varies with the threshold value. In this case, both simulation models yield bubble frequencies around $1\,s^{-1}$ for $th = 0.3$, while they lead to frequencies around $3 - 4\,s^{-1}$ for $th = \bar{\theta}_p$.

The spectra of absolute pressure, differential pressure and particle volume fraction obtained with CPFD-Barracuda resemble

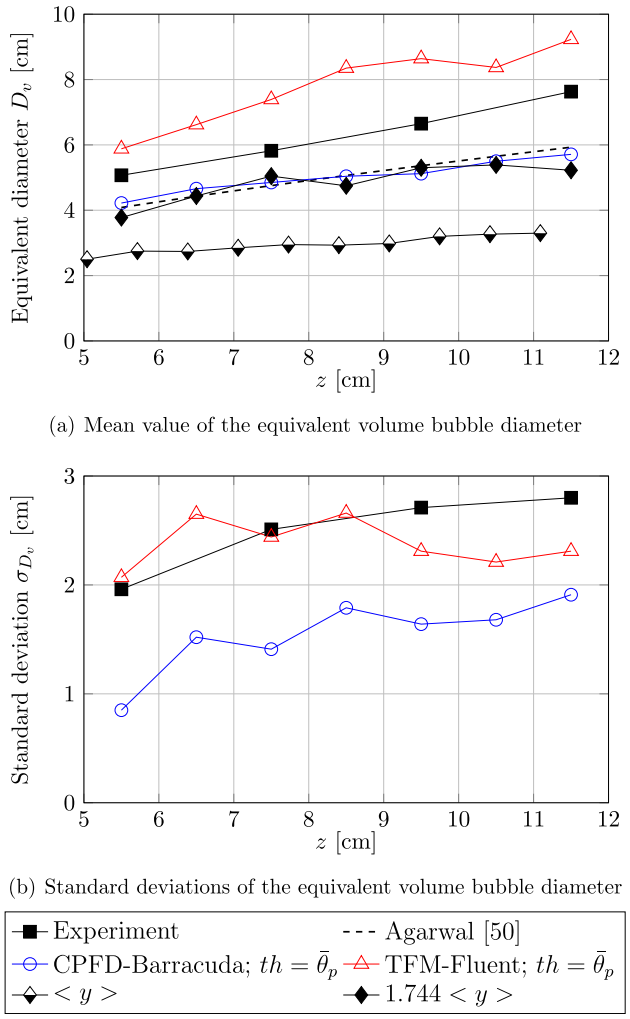


(a) Mean value of the equivalent volume bubble diameter

(b) Standard deviations of the equivalent volume bubble diameter

**Fig. 15.** Mean value (a) and standard deviation (b) of the bubble size for different bed heights at $r/R = 0.8$.

those from the experiments and the TFM-Fluent simulations, but with a larger contribution of lower frequencies. The peaks of the spectrum of particle volume fraction from CPFD-Barracuda are located at lower frequencies than the differential pressure ones. This suggests a high frequency filtering in the particle volume fraction results from CPFD-Barracuda.

The *PDF* obtained with both numerical models for $\bar{y}$ and $D_v$ and $u_b$ with $th = \bar{\theta}_p$ are similar to those obtained experimentally, although the CPFD-Barracuda distributions are closer to the experimental ones than the TFM-Fluent distributions. The equivalent diameter and velocities of the bubbles calculated with $th = \bar{\theta}_p$ by TFM-Fluent are higher than the experimental ones, while those calculated by CPFD-Barracuda are lower. In general, for the experimental conditions of this work, CPFD-Barracuda predicts smaller bubbles with lower velocities than TFM-Fluent.

The above results show that CPFD-Barracuda is, in general, able to predict the behaviour of bubbling beds with reasonable accuracy and with a computational cost of, approximately, 30 h to simulate 60 s of real time operation.

## 6. Notation

*CFL* Courant-Friedrichs Lewy
$C_d$ Gas-particle drag coefficient
*CFD* Computational fluid dynamics
*CPFD* Computational particle fluid dynamic
*DEM* Discrete element models
$D_p$ Drag function
$D_v$ Volume equivalent bubble diameter
$D_{wy}$ Wen-Yu model drag force
$d_p$ Particle diameter
$e_{mass}$ Error in the initial mass
$F$ Momentum exchange rate per volume between gas and particles
*FCC* Fluid catalytic cracking
$F_p$ Drag force exerted on the particle
$H_{bed}$ Initial bed height
$m_p$ Mass of the particle
$m_{sim}$ Simulated initial particle mass
$m_{theo}$ Theoretical initial particle mass
*MP − PIC* Multiphase particle in cell
$p$ Pressure
$P_s$ Pressure constant
*PDF* Probability density function
*PSD* Power spectral density
$R$ Radius of the bed
$R_g$ Gas constant
*Re* Reynolds number
$T$ Absolute temperature
*TFM* Two-fluid models
*th* Threshold
$u_b$ Time averaged bubble velocity
$u_f$ Fluid velocity
$u_p$ Particle velocity
$u_{mf}$ Minimum fluidization velocity
$V_p$ Particle volume
$y$ Pierced length
$\bar{y}$ Mean pierced length

### 6.1. Greek symbols

$\tau_p$ Stress tensor
$\theta_p$ Particle volume fraction
$\bar{\theta}_p$ Average particle volume fraction
$\beta$ Constant
$\theta_{cp}$ Particle volume fraction at close packing
$\varepsilon$ Constant
$\mu_f$ Dynamic fluid viscosity
$\rho_f$ Fluid density
$\rho_p$ Particle density
$\Psi_p$ Sphericity
$\theta_f$ Fluid volume fraction
$\bar{\theta}_p$ Time averaged particle volume fraction
$\tau_f$ Viscous stress term

## Declaration of Competing Interest

The authors declare that they have no known competing financial interests or personal relationships that could have appeared to influence the work reported in this paper.

## Acknowledgments

This work was partially funded by the *Ministerio de Economía y Competitividad* (Projects ENE2016-78908-R and RTI2018-096664-B-C21 (MICINN, FEDER/UE)) of the Spanish Government, the Regional Government of Castilla-La Mancha (project SBPLY/17/

180501/000412) and the *Ministerio de Ciencia, Innovación y Universidades - Agencia Estatal de Investigación (AEI)* (RED2018–102431-T).

## References


[1] P. Basu, Combustion and gasification in fluidized beds, CRC Press, 2006.
[2] D. Kunii, O. Levenspiel, Fluidization Engineering, Elsevier, 2013.
[3] A. Gómez-Barea, B. Leckner, Modeling of biomass gasification in fluidized bed, Prog. Energy Combust. Sci. 36 (2010) 444–509.
[4] A. Burggraeve, T. Monteyne, C. Vervaet, J.P. Remon, T. De Beer, Process analytical tools for monitoring, understanding, and control of pharmaceutical fluidized bed granulation: a review, European journal of Pharmaceutics and Biopharmaceutics 83 (2013) 2–15.
[5] J.A. Almendros-Ibáñez, M. Fernández-Torrijos, M. Díaz-Heras, J.F. Belmonte, C. Sobrino, A review of solar thermal energy storage in beds of particles: packed and fluidized beds, Sol. Energy 192 (2019) 193–237.
[6] S. Karimipour, T. Pugsley, Application of the particle in cell approach for the simulation of bubbling fluidized beds of Geldart A particles, Powder Technol. 220 (2012) 63–69.
[7] V. Mathiesen, T. Solberg, B.H. Hjertager, Predictions of gas/particle flow with an eulerian model including a realistic particle size distribution, Powder Technol. 112 (2000) 34–45.
[8] J.R. Grace, F. Taghipour, Verification and validation of CFD models and dynamic similarity for fluidized beds, Powder Technol. 139 (2004) 99–110.
[9] G. Ferschneider, P. Mege, Eulerian simulation of dense phase fluidized beds, Revue de L'institut Francais du Petrole 51 (1996) 301–307.
[10] J. Bayle, P. Mege, T. Gauthier, Dispersion of bubble flow properties in a turbulent FCC fluidized bed, Fluidization X (2001) 125–132.
[11] J. Grace, G. Sun, Influence of particle size distribution on the performance of fluidized bed reactors, The Canadian Journal of Chemical Engineering 69 (1991) 1126–1134.
[12] A. Acosta-Iborra, C. Sobrino, F. Hernández-Jiménez, M. De Vega, Experimental and computational study on the bubble behavior in a 3-D fluidized bed, Chem. Eng. Sci. 66 (2011) 3499–3512.
[13] A. Nikolopoulos, A. Stroh, M. Zeneli, F. Alobaid, N. Nikolopoulos, J. Ströhle, S. Karellas, B. Epple, P. Grammelis, Numerical investigation and comparison of coarse grain CFD–DEM and TFM in the case of a 1 MWth fluidized bed carbonator simulation, Chem. Eng. Sci. 163 (2017) 189–205.
[14] W. Wang, Y. Chen, Advances in Chemical Engineering, volume 47, Academic Press, pp. 193–277.
[15] N. Deen, M.V.S. Annaland, M.A. Van der Hoef, J. Kuipers, Review of discrete particle modeling of fluidized beds, Chem. Eng. Sci. 62 (2007) 28–44.
[16] L. Zhang, Z. Wang, S. Li, H. Qin, Effect of a draft tube on oil shale particle drying process of a spouted bed: CPFD simulation studies, Adv. Powder Technol. 29 (2018) 2255–2267.
[17] A. Nikolopoulos, K. Atsonios, N. Nikolopoulos, P. Grammelis, E. Kakaras, An advanced EMMS scheme for the prediction of drag coefficient under a 1.2 MWth CFBC isothermal flow – Part II: Numerical implementation, Chem. Eng. Sci. 65 (2010) 4089–4099.
[18] A. Muhammad, N. Zhang, W. Wang, CFD simulations of a full-loop CFB reactor using coarse-grained Eulerian-Lagrangian dense discrete phase model: effects of modeling parameters, Powder Technol. 354 (2019) 615–629.
[19] M. Adnan, J. Sun, N. Ahmad, J.J. Wei, Verification and validation of the DDPM-EMMS model for numerical simulations of bubbling, turbulent and circulating fluidized beds, Powder Technol. 379 (2021) 69–88.
[20] D. Snider, An incompressible three-dimensional multiphase particle-in-cell model for dense particle flows, J. Comput. Phys. 170 (2001) 523–549.
[21] H.P. Zhu, Z.Y. Zhou, R.Y. Yang, A.B. Yu, Discrete particle simulation of particulate systems: theoretical developments, Chem. Eng. Sci. 62 (2007) 3378–3396.
[22] D.M. Snider, S.M. Clark, P.J. O'Rourke, Eulerian–lagrangian method for three-dimensional thermal reacting flow with application to coal gasifiers, Chem. Eng. Sci. 66 (2011) 1285–1295.
[23] Y. Liang, Y. Zhang, T. Li, C. Lu, A critical validation study on CPFD model in simulating gas–solid bubbling fluidized beds, Powder Technol. 263 (2014) 121–134.
[24] C.B. Solnordal, V. Kenche, T.D. Hadley, Y. Feng, P.J. Witt, K.-S. Lim, Simulation of an internally circulating fluidized bed using a multiphase particle-in-cell method, Powder Technol. 274 (2015) 123–134.
[25] B.D. Adkins, N. Kapur, T. Dudley, S. Webb, P. Blaser, Experimental validation of cfd hydrodynamic models for catalytic fast pyrolysis, Powder Technol. 316 (2017) 725–739.
[26] A. Lanza, M.A. Islam, H. de Lasa, CPFD modeling and experimental validation of gas–solid flow in a down flow reactor, Comput. Chem. Eng. 90 (2016) 79–93.
[27] S. Kraft, M. Kuba, F. Kirnbauer, K. Bosch, H. Hofbauer, Optimization of a 50 MW bubbling fluidized bed biomass combustion chamber by means of computational particle fluid dynamics, Biomass Bioenergy 89 (2016) 31–39.
[28] M. Nakhaei, C.E. Hessel, H. Wu, D. Grévain, S. Zakrzewski, L.S. Jensen, P. Glarborg, K. Dam-Johansen, Experimental and CPFD study of gas–solid flow in a cold pilot calciner, Powder Technol. 340 (2018) 99–115.
[29] S. Wang, K. Luo, C. Hu, L. Sun, J. Fan, Impact of operating parameters on biomass gasification in a fluidized bed reactor: An eulerian-lagrangian approach, Powder Technol. 333 (2018) 304–316.
[30] X. Shi, X. Lan, F. Liu, Y. Zhang, J. Gao, Effect of particle size distribution on hydrodynamics and solids back-mixing in CFB risers using CPFD simulation, Powder technology 266 (2014) 135–143.
[31] Y. Wu, X. Shi, Y. Liu, C. Wang, J. Gao, X. Lan, 3D CPFD simulations of gas-solids flow in a CFB downer with cluster-based drag model, Powder Technol. 361 (2020) 400–413.
[32] J. Chladek, C.K. Jayarathna, B.M. Moldestad, L.-A. Tokheim, Fluidized bed classification of particles of different size and density, Chem. Eng. Sci. 177 (2018) 151–162.
[33] W.S. Amarasinghe, C.K. Jayarathna, B.S. Ahangama, L.-A. Tokheim, B.M.E. Moldestad, Experimental study and CFD modelling of minimum fluidization velocity for geldart A, B and D particles (2017).
[34] J.-H. Lim, K. Bae, J.-H. Shin, J.-H. Kim, D.-H. Lee, J.-H. Han, D.H. Lee, Effect of particle–particle interaction on the bed pressure drop and bubble flow by computational particle-fluid dynamics simulation of bubbling fluidized beds with shroud nozzle, Powder Technol. 288 (2016) 315–323.
[35] S. Yang, H. Wu, W. Lin, H. Li, Q. Zhu, An exploratory study of three-dimensional mp-pic-based simulation of bubbling fluidized beds with and without baffles, Particuology 39 (2018) 68–77.
[36] F. Hernández-Jiménez, S. Sánchez-Delgado, A. Gómez-García, A. Acosta-Iborra, Comparison between two-fluid model simulations and particle image analysis & velocimetry (PIV) results for a two-dimensional gas–solid fluidized bed, Chem. Eng. Sci. 66 (2011) 3753–3772.
[37] H. Shi, A. Komrakova, P. Nikrityuk, Fluidized beds modeling: Validation of 2D and 3D simulations against experiments, Powder Technol. 343 (2019) 479–494.
[38] C. Sobrino, A. Acosta-Iborra, M. Izquierdo-Barrientos, M. De Vega, Three-dimensional two-fluid modeling of a cylindrical fluidized bed and validation of the maximum entropy method to determine bubble properties, Chem. Eng. J. 262 (2015) 628–639.
[39] I.A. Fluent, User Guide, Ansys Inc., Canonburg, PA, USA, 2016.
[40] T.B. Anderson, R. Jackson, Fluid mechanical description of fluidized beds. equations of motion, Industrial & Engineering Chemistry Fundamentals 6 (1967) 527–539.
[41] C.Y. Wen, Y.H. Yu, Mechanics of fluidzation, AIChE Symp. Ser. 62 (1966) 100–111.
[42] M. Sommerfeld, N. Huber, Experimental analysis and modelling of particle-wall collisions, International journal of multiphase flow 25 (1999) 1457–1489.
[43] J.A. Almendros-Ibáñez, S. Sánchez-Delgado, C. Sobrino, D. Santana, Experimental observations on the different mechanisms for solid ejection in gas-fluidized beds, Chem. Eng. Process. 48 (2009) 734–744.
[44] C. Sobrino, J.A. Almendros-Ibáñez, D. Santana, C. Vázquez, M. De Vega, Maximum entropy estimation of the bubble size distribution in fluidized beds, Chem. Eng. Sci. 64 (2009) 2307–2319.
[45] F. Johnsson, R. Zijerveld, J.v. Schouten, C. Van den Bleek, B. Leckner, Characterization of fluidization regimes by time-series analysis of pressure fluctuations, Int. J. Multiph. Flow 26 (2000) 663–715.
[46] J.C. Bandara, R. Thapa, H.K. Nielsen, B.M.E. Moldestad, M.S. Eikeland, Circulating fluidized bed reactors–part 01: analyzing the effect of particle modelling parameters in computational particle fluid dynamic (CPFD) simulation with experimental validation, Part. Sci. Technol. (2020) 1–14.
[47] J. Werther, Bubbles in gas fluidized-beds. 1, Transactions of the Institution of Chemical Engineers 52 (1974) 149–159.
[48] K. Pal, J. Theuerkauf, Multiphase particle in cell simulations of fluidized beds: Studies on bubble rise velocity and minimum fluidization velocity, Chem. Ing. Tech. 93 (2021) 237–246.
[49] D. Santana, J. Rodríguez-Rodríguez, J.A. Almendros-Ibáñez, C. Martínez-Bazán, Characteristic lengths and maximum entropy estimation from probe signals in the ellipsoidal bubble regime, Int. J. Multiph. Flow 32 (2006) 1123–1139.
[50] P. Agarwal, Bubble characteristics in gas fluidized beds, Chemical Engineering Research & Design 63 (1985) 323–337.
[51] S. Karimipour, T. Pugsley, A critical evaluation of literature correlations for predicting bubble size and velocity in gas–solid fluidized beds, Powder Technol. 205 (2011) 1–14.
[52] M. Rüdisüli, T.J. Schildhauer, S.M. Biollaz, J.R. van Ommen, Monte carlo simulation of the bubble size distribution in a fluidized bed with intrusive probes, Int. J. Multiph. Flow 44 (2012) 1–14.